A stochastic model based on Gaussian random fields to characterize the morphology of granular objects

Léo Théodon, Carole Coufort-Saudejaud, Johan Debayle

Pattern Recognition 149 (2024) 110255

Contents lists available at ScienceDirect

Pattern Recognition

journal homepage: www.elsevier.com/locate/pr

A stochastic model based on Gaussian random fields to characterize the morphology of granular objects

L. Théodon [a,*], C. Coufort-Saudejaud [b], J. Debayle [a]

[a] MINES Saint-Etienne, CNRS, UMR 5307 LGF, Centre SPIN, Saint-Etienne, France
[b] Laboratoire de Génie Chimique, Université de Toulouse, CNRS, INPT, UPS, Toulouse, France

ARTICLE INFO

Keywords:
3D modeling
Aggregate
Agglomerate
Fourier descriptor
Gaussian random fields
Image analysis
Morphological characterization

ABSTRACT

The geometrical modeling of granular objects is a complex challenge that exists in many scientific fields, such as the modeling of granular materials or rocks and coarse aggregates with applications in civil, mechanical, and chemical engineering. In this paper, a model called SPHERE (Stochastic Process for Highly Effective Radial Expansion) is proposed, which is based on the deformation of an ellipsoid mesh using multiple 3D Gaussian random fields. The model is designed to be flexible (full control over 2D and 3D morphological properties of granular objects), ultra-fast (over 1000 aggregates in less than 5 s), and independent of the mesh and base shape used (as long as it is a star-shaped object). The flexibility of the model and its ability to reflect real data is illustrated using images of latex nanoparticle aggregates. Using 2D measurements on images from a morphogranulometer, a method based on the SPHERE model is proposed to estimate the 3D morphological properties of aggregates. A multiscale optimization process is applied, in particular using a partial reconstruction of 2D shapes from elliptic Fourier descriptors, in order to best reproduce the shape, angularity and texture of the aggregates using the SPHERE model. Validation of the method on 3D printed data shows relative errors of less than 3% for all measured 2D and 3D morphological characteristics, and validation on a population of synthetic objects shows relative errors of less than 6%. The results are compared and discussed with those obtained using other models based on overlapping spheres and show consistency with previous work. Finally, suggestions for improvement are given.

1. Introduction

The morphological characterization of granular objects, aggregates or agglomerates is a key concern in many fields, from the pharmaceutical [1,2] and food industries [3,4] to the chemical industry [5,6] and civil engineering [7,8]. In fact, the morphology of these objects is directly related to their physico-chemical or mechanical properties, and consequently to their taste quality [4] , toxicity [9], health and environmental hazards [10,11], or even to their mechanical strength [12]. For all these reasons, the modeling of these objects, coupled with image analysis techniques to determine their morphological characteristics, has become a major concern. In fact, image analysis alone provides only partial information about the analyzed objects, and in most cases it provides two-dimensional information. Using a model and fitting it to real data can then, under certain hypotheses, complement the information obtained from image analysis by estimating certain 3D morphological characteristics such as volume or surface area. This approach has been used in previous work [13], for example, using images from a morphogranulometer and assuming a certain cylindrical symmetry of the observed objects.

The difficulty in implementing such methods lies not only in the number of assumptions that must be made in order to estimate 3D properties from 2D information, but also in choosing a model that is flexible enough to be representative of real data, yet efficient and easily tunable. In fact, when it comes to modeling aggregates, agglomerates, or granular objects in general, there are numerous models available. Models based on overlapping spheres are particularly popular for modeling aerosols or soot aggregates [14–17], but more generally for modeling any type of granular object, compact or not (Moreaud et al. [18]). The morphological properties of objects generated in this way can usually be easily adjusted using model parameters. The main drawbacks, however, are their relative slowness in terms of computation time and the difficulty of accurately describing the fine surface texture of granular objects, such as sand grains, without unreasonably increasing the number of spheres required (Ferellec and McDowell [19]).

Another popular technique is to generate random shapes from Fourier descriptors. This is especially useful for 2D objects (Mollon

* Corresponding author.
E-mail addresses: l.theodon@emse.fr (L. Théodon), carole.saudejaud@toulouse-inp.fr (C. Coufort-Saudejaud), debayle@emse.fr (J. Debayle).

https://doi.org/10.1016/j.patcog.2024.110255
Received 25 October 2023; Received in revised form 11 December 2023; Accepted 2 January 2024
Available online 5 January 2024

and Zhao [20] and Chen et al. [21]), but also for 3D objects (Mollon and Zhao [22]). In the 3D case, Mollon and Zhao [23] also suggests using a combination of periodic 2D Gaussian random fields instead of Fourier harmonics to apply deformations of varying intensity and scale to a sphere. Furthermore, a three-dimensional description of the surface of a 3D object, analogous to Fourier descriptors in two-dimensional analysis, are spherical harmonics (Baxansky and Kiryati [24]). As a result, a large number of models for the generation of random objects have been developed using this approach (Garboczi and Bullard [25], Wei et al. [26] and Ueda [27]). However, while these methods are very flexible and efficient compared to overlapping sphere models, they have the disadvantage of requiring a very large number of parameters (often several dozen), depending on the level of detail required to describe an object, which is particularly problematic in the context of an optimization process due to the curse of dimensionality [28].

Therefore, this article proposes a new model called SPHERE (Stochastic Process for Highly Effective Radial Expansion) for granular object generation. The idea is to deform a basic object using different 3D Gaussian random fields to influence the different morphological properties of the object (shape, angularity, texture). In the context of this work, two random fields are used to deform an ellipsoid, bringing the total number of model parameters to 6 and making it much easier to fit to real data. Furthermore, using 3D random fields to deform the object makes the method extremely easy to implement and completely independent of the mesh used. In particular, there are no longer any periodicity constraints to impose on the random field, which is often a difficulty when using such techniques, whether using Gaussian fields (Mollon and Zhao [23]) or other spherical random noise (Spjut et al. [29] and Hettinga et al. [30]). Finally, generating the 3D Gaussian random fields using a Fourier transform makes the whole process extremely efficient, with over 1000 objects generated in just 5 s using optimized standard MATLAB® code.

In summary, the original contributions are as follows

1. A model for generating granular objects based on multiple 3D random fields to take into account the multi-scale aspect of the morphological descriptors.
2. The independence of the model from the choice of mesh (see Appendix), the speed of object generation and the flexibility of the model with a limited number of parameters.
3. The validation of the method on real objects and on a population of synthetic objects using a multiscale optimization process based on partial reconstructions of 2D projections using elliptic Fourier descriptors (Kuhl and Giardina [31] and Crampton [32]). The application of the method to latex nanoparticle aggregates.

In the following section, the aim of this work, i.e. the characterization of latex nanoparticle aggregates from 2D images, is described and the main morphological characteristics measured are presented. The SPHERE model is then described and examples of randomly generated objects are shown. The optimization process for fitting model parameters to real data is then described, and the model is validated on calibrated real objects, namely 3D printed aggregates, and on numerical data (see Section 4.2). Finally, the method is applied to real data, i.e. aggregates obtained from agglomeration experiments of Hamieh et al. [33] (see Section 5). The results are discussed and prospects for future work are provided.

2. The proposed method

From an experimental point of view, the real materials studied in this article are 3D printed aggregates and aggregates obtained from the agglomeration of latex nanoparticles by Hamieh et al. [33] (see Section 5.1). For both types of real aggregates, several images were taken at the end of the aggregation process using a morphogranulometer (Morphologi G3 - Malvern Panalytical). However, only 2D characteristics were measured by image analysis, so the current work aims to go a step further by also covering 3D characteristics.

Table 1
List of morphological characteristics used in this paper.

Parameter	Symbol	Definition and equation
Feret diameter max.	$F_{\max}$	Longest caliper (Feret) length
Feret diameter min.	$F_{\min}$	Smallest caliper (Feret) length
2D parameters		
Projected area	A	Area of the object
Convex area	A_c	Area of the convex hull
Perimeter	P	length of the object outline
Equivalent Circle Diameter	ECD	$2\times\sqrt{A/\pi}$
Projected major axis	a_p	Major axis of the equivalent ellipse
Projected minor axis	b_p	Minor axis of the equivalent ellipse
Projected elongation	e_p	b_p/a_p
Aspect ratio	AR	$F_{\min}/F_{\max}$
Convexity	Co	A/A_c
Circularity	C	$4\pi\times A/P^2$
3D parameters		
Volume	V	Volume of the object
Convex volume	V_c	Volume of the convex hull
Surface area	S	Area of the object surface
Equivalent Sphere Diameter	ESD	$2\times\sqrt[3]{3\times V/(4\pi)}$
Major axis	a	Major axis of the basic shape
Minor axis	b	Minor axis of the basic shape
Elongation	e	b/a
Solidity	SLD	V/V_c
Sphericity	Φ_S	$6\pi^2\times V/(\sqrt{\pi}S)^3$

The characterization of aggregates or agglomerates using image analysis is a rapidly growing topic, especially as new deep learning techniques have emerged in recent years (Frei and Kruis [34], Monchot et al. [35], Rühle et al. [36] and Lins et al. [37]). However, one of the most important issues is the choice of the characteristics to be measured. In fact, several dozen morphological characteristics can be defined to characterize 2D or 3D shapes, and their relevance can vary greatly depending on the context, the type of object considered, the imaging device, or the scale considered (Théodon et al. [38]).

When it comes to latex nanoparticle aggregates, in addition to projected area, perimeter and Equivalent Circle Diameter (ECD), which are size characteristics, *convexity* and *circularity* are appropriate descriptors. In fact, these are shape and angularity features that not only help to describe the geometry of the aggregates, but can also be related to their physicochemical properties, as well as to parameters of the aggregation process itself, as Guérin et al. [39,40] has shown in previous work. The *convexity* is the ratio of the projected area to the convex area, and the *circularity* is a measure of how close a geometric shape is to a circle. Since these are 2D morphological properties, their 3D equivalents - *solidity* and *sphericity*, respectively — are also measured on 3D objects derived from the SPHERE model. Similarly, the 3D equivalent of EDC, the Equivalent Sphere Diameter (ESD), will be the main size criterion. Table 1 provides an exhaustive list of all the morphological characteristics used in the remainder of this article.

Thus, the proposed method aims at estimating the 3D characteristics of latex nanoparticle aggregates using a stochastic geometric model, where the model parameters are adjusted by matching the 2D characteristics of the synthetic objects generated by the model with those measured on images from the morphogranulometer. Once an optimal parameterization of the model is found, the 3D properties of the synthetic aggregates are measured and used as an estimate of the 3D properties of the real aggregates. This model-based approach is proposed because each of the aggregates is only visible in a single image, and methods based on multiple images (Grum and Bors [41], Kang et al. [42] and Yan et al. [43]), for example, are not applicable.

3. The sphere model

Mesh deformation can be efficiently performed using pseudo-random noise such as Perlin (Hettinga et al. [30]), Simplex (Spjut et al.

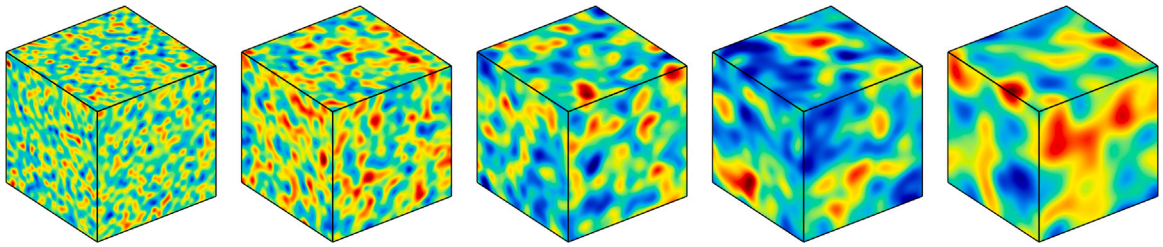

(a) $\ell = 1$ (b) $\ell = 2$ (c) $\ell = 5$ (d) $\ell = 10$ (e) $\ell = 25$

Fig. 1. Example of 3D Gaussian random fields generated on a 50^3 px^3 grid with different chord lengths ℓ and with the correlation function given by Eq. (1). Colors represent field intensity (dark blue = 0 and dark red = 1). (For interpretation of the references to color in this figure legend, the reader is referred to the web version of this article.)

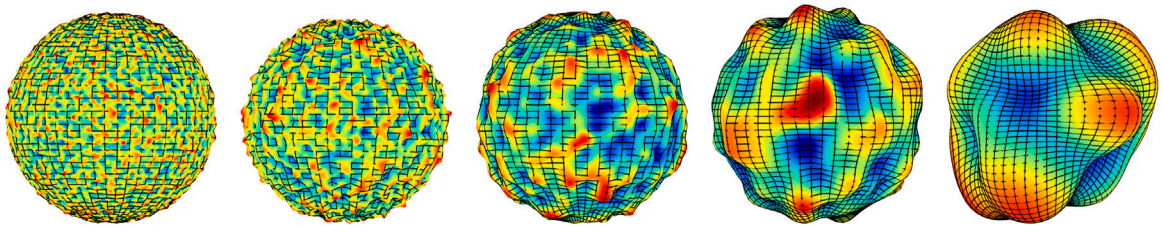

(a) $\ell = 1, c = 0.05$ (b) $\ell = 2, c = 0.1$ (c) $\ell = 5, c = 0.15$ (d) $\ell = 10, c = 0.2$ (e) $\ell = 25, c = 0.5$

Fig. 2. Example of deformation of the mesh of a sphere by 3D Gaussian random fields generated on a 50^3 px^3 grids with different chord lengths ℓ and with the correlation function given by Eq. (1).

[29]), or Open-Simplex. However, these methods can be complex to implement and generally lead to an inflation in the number of parameters. In addition, pseudo-randomness is not necessarily desirable when generating a random object. Therefore, using random fields (Mollon and Zhao [23]) such as Markovian random fields or Gaussian random fields to deform a mesh is a good alternative. These random fields are generally assumed to be isotropic, homogeneous, and stationary. In this case, the generation of Gaussian random fields is particularly efficient thanks to methods based on the Fast Fourier Transform (FFT).

However, the deformation of spherical objects using random fields requires the generation of periodic fields or the imposition of edge conditions, which can be complex to implement (Mollon and Zhao [23]). To overcome these limitations, a model called SPHERE (Stochastic Process for Highly Effective Radial Expansion) is proposed. This model is based on the use of 3D random fields to deform a spherical or ellipsoidal mesh, making this deformation particularly efficient in terms of computational time, completely independent of the mesh (see Appendix), and completely free of object periodicity constraints. This section explains the algorithm for efficiently generating 3D random Gaussian fields and introduces the SPHERE model.

The use of a Gaussian random field offers several major advantages, such as ultra-fast generation compared to that of a Markovian random field, for example, due to the use of an FFT-based algorithm, and complete determination of the field from a covariance function that, in the context of this article, depends on only one parameter, the chord length. Limiting the number of parameters is critical when applying the optimization process to the model. These points will be discussed in detail in the following sections.

3.1. Generation of a 3D Gaussian random field

An efficient method for generating a 3D Gaussian field is based on the work of Adler et al. [44] and Liang et al. [45], who express the random field as the convolution of an uncorrelated Gaussian random noise with a symmetric and normalized weight function. Lang and Potthoff [46] then shows that avoiding the computation of the convolution product by going into the Fourier space not only speeds up the computation considerably, but also results in extremely low error.

The process of generating a 3D Gaussian random field using an FFT can be described as follows:

1. A covariance function $C(\vec{r})$, such as an exponential quadratic kernel (also known as a Radial Basis Function or RBF kernel), must be defined.
$$C(\vec{r}) = \exp\left(\frac{\|\vec{r}^2\|}{2\ell^2}\right) \tag{1}$$
with $\vec{r} = (x, y, z) \in \mathbb{R}^3$ and ℓ a scale length called *chord length*.
2. The spectral power function $\widehat{C}(\vec{k})$ is defined as the Fourier transform of the covariance.
$$\widehat{C}(\vec{k}) = FFT\left(C(\vec{r})\right) \tag{2}$$
3. The Gaussian random field $G(\vec{r})$ is obtained by applying the inverse Fourier transform to the product of the square root of $\widehat{C}(\vec{k})$ and the Fourier transform $\widehat{\mathcal{N}}(\vec{k})$ of an uncorrelated Gaussian random noise $\mathcal{N}(\vec{r})$.
$$G(\vec{r}) = FFT^{-1}\left[\widehat{\mathcal{N}}(\vec{k}) \times \sqrt{\widehat{C}(\vec{k})}\right] \tag{3}$$

This method is particularly effective for fast 3D random field generation. For example, on a machine equipped with an Intel(R) Core(TM) i9-12900KF processor at 3.19 GHz and 64 GB of RAM using MATLAB® (2023b), it takes about 10^{-2} s to generate a 3D Gaussian random field on a 50^3 px^3 grid, which is the size that will be used to deform the mesh of spheres or ellipsoids in the remainder of this paper. In particular, Fig. 3 shows the evolution of the computational time required to generate a 3D Gaussian random field on grids of different sizes.

Finally, a Gaussian random field is completely determined by its covariance function, and in particular by the chord length ℓ. Fig. 1 illustrates the influence of this parameter on the structure of the random field.

3.2. Mesh deformation using a 3D Gaussian random field

The proposed method for generating random 3D objects is based on the deformation of a 3D mesh using a 3D Gaussian random field. The method can be described as follows:

1. A mesh M corresponding to a set of points in $\mathbb{R}^3$ is generated; for example, a sphere, an ellipsoid, or any convex object.

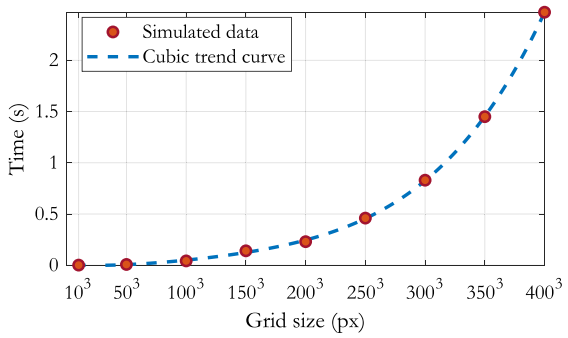

Fig. 3. Time required to generate a 3D Gaussian random field on grids of different sizes using the previous algorithm. The simulated data are averaged over 20 simulations.

2. A 3D Gaussian random field $G(\vec{r})$ with normalized values in $[-1;1]$ is generated.
3. Each point $\vec{r} = (x, y, z) \in M$ of the mesh is affected by the displacement $c \times G(\vec{r}) \times \vec{n}$, where $\vec{n}$ is the mesh normal and $c \in [0;1]$ is an intensity coefficient.

Since the Gaussian field $G(\vec{r})$ is discretized, its value at any point in space is calculated by cubic spline interpolation. Fig. 2 shows the results of deforming a sphere mesh with Gaussian fields of different chord lengths ℓ and for different intensity coefficients c.

Unlike most conventional methods that use 2D random fields as displacement maps to deform 3D objects or surfaces [29,30,47], the proposed method uses 3D Gaussian random fields, which means that no periodicity problems arise and it is independent of the meshing of the shape under consideration (see Appendix), i.e. in this case a sphere or an ellipsoid. Although the computation time of a 3D random field is much higher than that of a 2D random field, in the context of the application proposed in this paper, this is negligible compared to the time required to compute the morphological characteristics of the generated 3D objects, which can take several tenths of a second.

3.3. The proposed model

3.3.1. Model description

The proposed model generates granular objects resembling compact aggregates from a combination of Gaussian random fields applied to the mesh of an ellipsoid. The idea is to rely on a classification hierarchy of common morphological characteristics. The basic object, the ellipsoid, is used to give it a basic *shape*. A first Gaussian random field G_A modifies the overall shape and acts on what is called *angularity*. Finally, a second Gaussian random field G_T is used to add small details to the surface, commonly referred to as the *texture* of the object. The generation process can be summarized as follows:

1. The mesh M of an ellipsoid with major axis a and equal minor axes b is generated.
2. Two 3D Gaussian random fields G_A and G_T are generated with chord lengths ℓ_A and ℓ_T, respectively, where $\ell_A > \ell_T$.
3. The mesh M is deformed by a combination G_C of the two random fields G_A and G_T, defined as follows:

$$G_C = c_A \times G_A + c_T \times G_T \tag{4}$$

where the coefficients c_A and c_T control the intensity of the deformation.

The proposed model thus depends on 6 parameters. Two parameters (a and b) control the size and general *shape* of the object, two parameters associated with the random field G_A (ℓ_A and c_A) control its *angularity*, and two parameters associated with the random field G_T (ℓ_T and c_T) control the surface *texture*. Fig. 5 illustrates the process of creating a 3D granular object, and Table 2 lists all 6 parameters used.

Table 2
List of the 6 parameters of the proposed model.

Parameter	Definition
a	Major axis
b	Minor axis
ℓ_A	Chord length of the random field G_A
ℓ_T	Chord length of the random field G_T
c_A	Deformation intensity factor with respect to G_A
c_T	Deformation intensity factor with respect to G_T

Limiting the model to two random fields and 6 parameters provides good flexibility while avoiding the curse of dimensionality found in models that use spherical harmonics (Garboczi and Bullard [25], Wei et al. [26] and Ueda [27]) or combine random fields and Fourier descriptors (Mollon and Zhao [23]), which can depend on more than 20 different parameters. Fig. 4 shows some examples of objects generated by the proposed model with different parameters.

3.3.2. Sensitivity of the parameters

Controlling the size and morphology of the objects generated by the model is a crucial issue when it comes to matching the measured morphological characteristics of simulated objects with those of real ones. In this section, the influence of model parameters on certain characteristics of size (volume V, projected major axis a_p), shape (elongation e), and angularity or texture (circularity C, sphericity Φ_S, solidity SLD) is examined.

In fact, since the objects studied here are generally based on 2D images captured with optical devices, half of the characteristics mentioned above are 2D characteristics. Indeed, while volume, the solidity (ratio of volume to convex volume), and the sphericity (a measure of the similarity of an object to a sphere) are indeed 3D characteristics, the projected major axis, elongation, and circularity (a measure of the similarity of a shape to a circle) are 2D characteristics, which in this case (e.g. for image acquisition with a morphogranulometer) are measured on a projection of the 3D object along a direction orthogonal to the maximum Feret diameter. In particular, the projected major axis and the elongation are calculated directly from the equivalent projected ellipse, as shown in Fig. 6.

The meshes of two objects are considered: one spherical (Fig. 7(a) with $b/a = 1$) and the other ellipsoidal (Fig. 7(b) with $b/a = 0.7$). The influence of the deformation intensity applied to these meshes by the two Gaussian random fields G_A (Fig. 7(c), $\ell_A = 25$) and G_T (Fig. 7(d), $\ell_T = 1$) is then studied by varying the coefficients c_A and c_T from 0 to 0.6.

Figs. 8 and 9 illustrate the influence of the model parameters on the 2D and 3D morphological characteristics for spherical and ellipsoidal base objects, respectively. When analyzing the results, it may be worth considering that, in the context of this work, the deformation intensity associated with the random field of angularity G_A generally does not exceed 0.3 to 0.4, and that associated with the random field of texture G_T is of the order of 0.05 to 0.1 at most.

- *Volume*: Regardless of the base object considered, the intensity coefficient c_A associated with the random field of angularity has a moderate effect on the volume of the object (generally less than 20% relative deviation), and the coefficient c_T associated with the random field of texture has a negligible effect.
- *Solidity & Sphericity*: No matter which base object is considered, the intensity coefficient c_A has a relatively small effect (less than 5% relative deviation in most cases), while the coefficient c_T has a considerable influence (quasi-linear for solidity, and similarly for sphericity up to an intensity of 0.35).

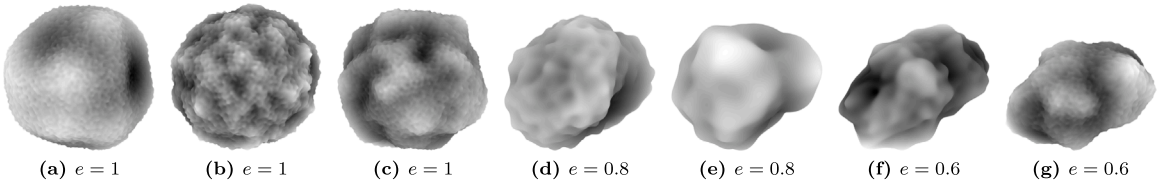

(a) $e = 1$ (b) $e = 1$ (c) $e = 1$ (d) $e = 0.8$ (e) $e = 0.8$ (f) $e = 0.6$ (g) $e = 0.6$

Fig. 4. Example of objects generated by the proposed model with different shapes, angularities and textures. The ratio $e = b/a$ ranges from 1 to 0.6, the deformation intensity applied by G_A is $c_A \in [0.05; 0.3]$ and that applied by G_T is $c_T \in [0.01; 0.10]$.

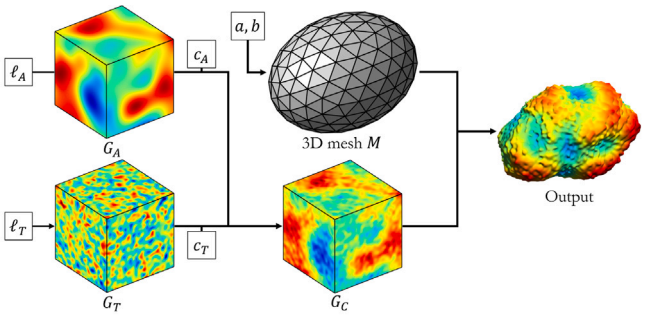

Fig. 5. Illustration of the process of generating granular objects using the proposed 6-parameter model.

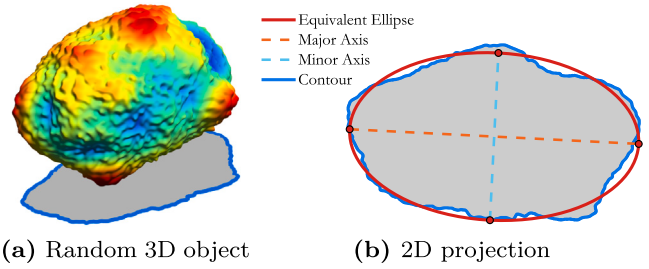

(a) Random 3D object (b) 2D projection

Fig. 6. Illustration of the calculation of the projected major axis a_p and minor axis b_p of the equivalent ellipse of the 2D projection of the 3D object along a direction orthogonal to the maximum Feret diameter.

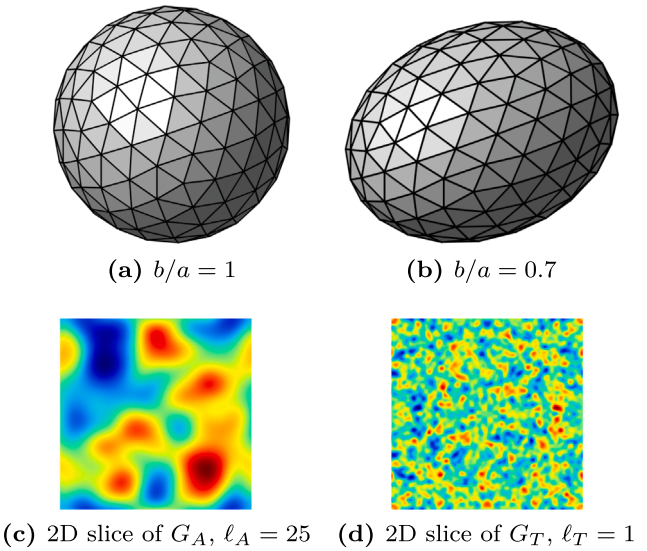

(a) $b/a = 1$ (b) $b/a = 0.7$

(c) 2D slice of G_A, $\ell_A = 25$ (d) 2D slice of G_T, $\ell_T = 1$

Fig. 7. Illustration of the parameterization used to show the influence of certain model parameters on the morphological characteristics of the generated objects. Figs. 7(a) and 7(b) show the basic shapes used in Figs. 8 and 9, respectively. Figs. 7(c) and 7(d) show cross-sections of the random fields G_A and G_T used to model *angularity* and *texture*, respectively.

- *Projected major axis*: Regardless of the base object considered, the intensity coefficients c_A and c_T both have a relatively small influence on the projected major axis of the equivalent ellipse (relative deviation of less than 10% up to a mesh deformation of 30%).
- *Elongation*: The relative deviation is negligible, except in the case of the intensity coefficient c_A for a spherical base object, with a relatively small overall influence (barely 10% relative deviation for a deformation of the order of 30%).
- *Circularity*: As with 3D sphericity, and whatever the base object considered, the influence of c_A is very weak (relative deviation of barely 10% for a deformation intensity of 0.6) and quite insignificant for c_T (relative deviation of practically 20% for a deformation intensity of 0.3).

In general, the results are in line with what might be expected, i.e. that the deformation intensity coefficient c_A associated with angularity acts mainly on the size of the object, through the volume and the projected major axis, as shown by the evolution of the means and the standard deviations, has a moderate effect on the elongation (cf. the standard deviations), and a rather small effect on the three other characteristics. Conversely, the deformation intensity coefficient associated with the texture c_T has a relatively small effect on the size and elongation characteristics, but a significant effect on the shape characteristics such as circularity, sphericity, and solidity, especially given its obvious effect on the surface of the object. Finally, it should not be forgotten that the parameters a and b, i.e. the major axis and the two minor axes of the base ellipsoid, have the greatest influence on the size and overall shape of the object (and especially on its elongation).

Finally, the fact that the projected major axis a_p and the elongation e, both calculated from the equivalent ellipse of the shape projected along an axis orthogonal to the maximum Feret diameter, make it relatively easy to estimate the mean values of the parameters a and b, assuming $a = a_p$ and $b = a_p \times e$, will prove particularly useful in the remainder of this paper when it comes to fitting the model parameters to real data.

3.3.3. Estimates and predictions

Figs. 8 and 9 show that the variance in solidity and sphericity as a function of the intensity coefficients c_A and c_T and the size parameters a and b (and thus the elongation ratio b/a of the basic shape) is extremely small. For this reason, these morphological characteristics can be predicted with relatively good accuracy from the model parameters using linear regression, as shown in Figs. 10(c) and 10(d).

The following empirical linear regression models are used for the solidity and sphericity:

$$\widehat{\mathrm{SLD}} = \alpha_0 + \alpha_1 \times c_T + \alpha_2 \times c_T \ell_T + \varepsilon \tag{5}$$

$$\widehat{\Phi}_S = \beta_0 + \beta_1 \times \frac{b}{a} + \beta_2 \times c_T + \beta_3 \times c_T \ell_T + \varepsilon \tag{6}$$

where α_0 and β_0 are the intercept terms and ε is the residual error. Similarly, two other linear regression models are suggested to estimate the normalized volume and surface area:

$$\widehat{V}_N = \gamma_0 + \gamma_1 \times \frac{b}{a} + \gamma_2 \times c_A \ell_A + \gamma_3 \times c_T \ell_T + \varepsilon \tag{7}$$

$$\widehat{S}_N = \eta_0 + \eta_1 \times \frac{b}{a} + \eta_2 \times c_T + \eta_3 \times c_T \ell_T + \varepsilon \tag{8}$$

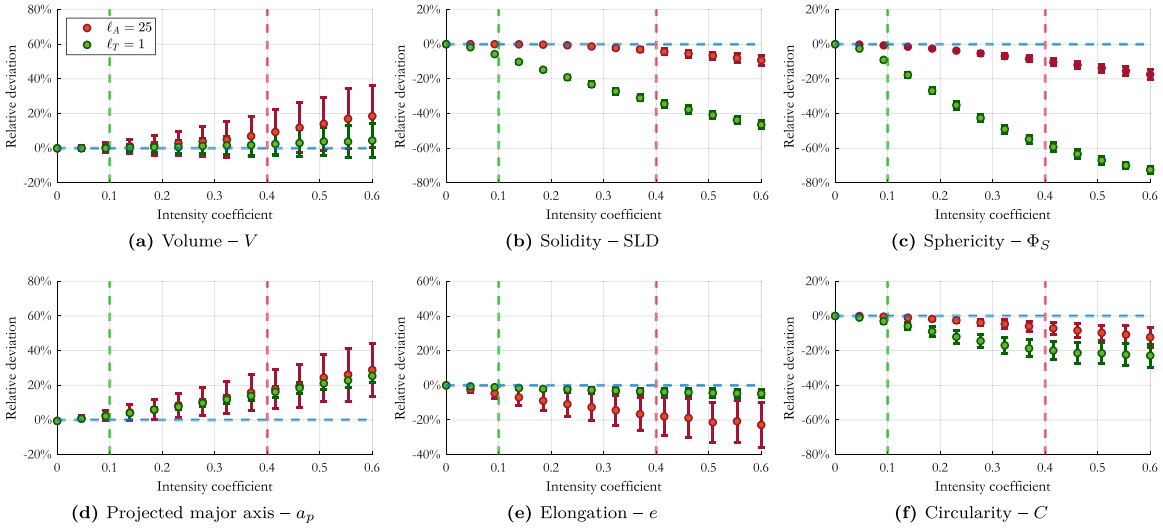

(a) Volume – V (b) Solidity – SLD (c) Sphericity – Φ_S

(d) Projected major axis – a_p (e) Elongation – e (f) Circularity – C

Fig. 8. Influence of intensity coefficients applied to the 3D Gaussian random fields G_A and G_T, which were generated with chord lengths of $\ell_A = 25$ and $\ell_T = 1$, respectively, and a ratio $b/a = 1$ (see Fig. 7(a)). The points represent the mean values calculated over 500 generated objects, and the bars represent ± one standard deviation.

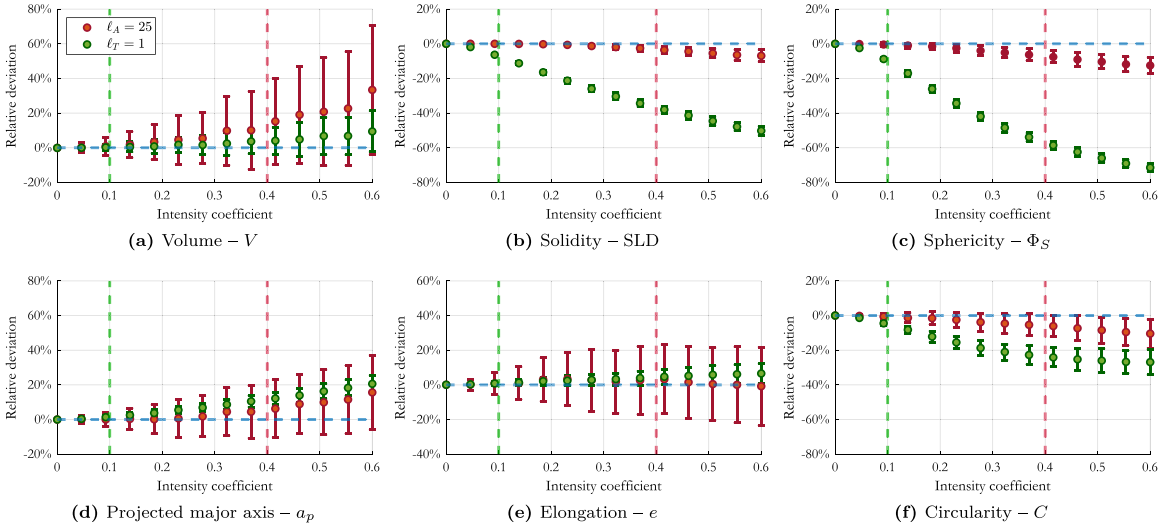

(a) Volume – V (b) Solidity – SLD (c) Sphericity – Φ_S

(d) Projected major axis – a_p (e) Elongation – e (f) Circularity – C

Fig. 9. Influence of intensity coefficients applied to the 3D Gaussian random fields G_A and G_T, which were generated with chord lengths of $\ell_A = 25$ and $\ell_T = 1$, respectively, and a ratio $b/a = 0.7$ (see Fig. 7(b)). The points represent the mean values calculated over 500 generated objects, and the bars represent ± one standard deviation.

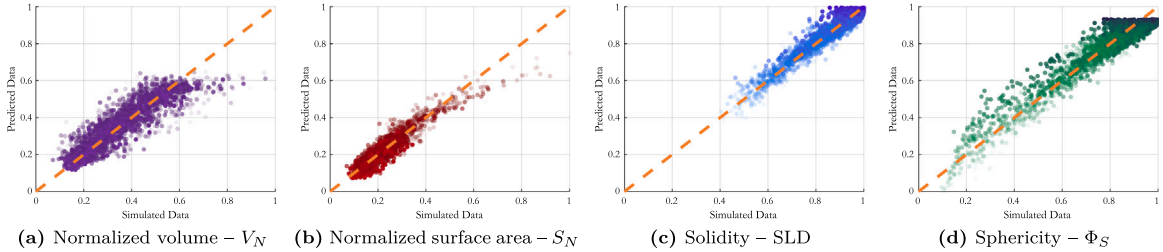

(a) Normalized volume – V_N (b) Normalized surface area – S_N (c) Solidity – SLD (d) Sphericity – Φ_S

Fig. 10. Simulated observed versus predicted data for the normalized volume, normalized surface area, solidity, and sphericity with linear regression models based on the proposed model parameters. Data are normalized. Darker dots indicate lower intensity coefficients c_A (Fig. 10(a)) and c_T (Figs. 10(b), 10(c) and 10(d)) and lighter dots indicate higher intensity coefficients. The simulated data set consists of 5000 observations.

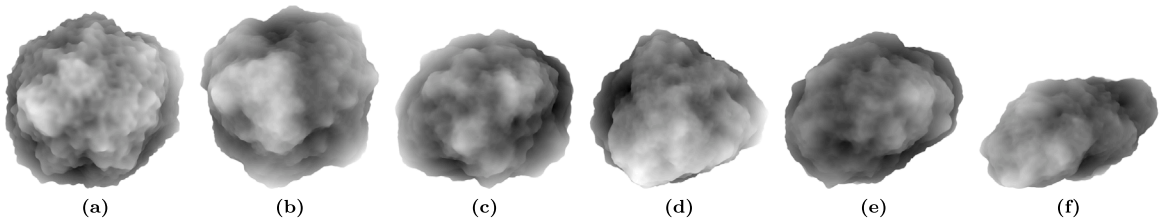

Fig. 11. Example of objects generated by extending the proposed model by using four Gaussian random fields instead of two.

Table 3
Intervals over which parameters are randomly and uniformly drawn to form linear regression training and testing datasets.

Parameter	a	b/a	ℓ_A	c_A	ℓ_T	c_T
Interval	[1; 10]	[0.1; 1]	[10; 25]	[0; 0.6]	[1; 10[	[0; 0.6]

Table 4
Adjusted $\bar{R}^2$ for the different linear regression models.

Characteristic	V_N	S_N	SLD	Φ_S
$\bar{R}^2$	0.740	0.861	0.919	0.915

where V_N and S_N are defined as follows:

$$V_N = V \times \left(\frac{4}{3}\pi ab^2\right)^{-1} \quad \text{and} \quad S_N = \frac{S}{S_{\text{ref}}} \tag{9}$$

and where S_{ref} is evaluated using Ramanujan's formula for calculating the surface area of an ellipsoid:

$$S_{\text{ref}} \approx 4\pi \left(\frac{2a^q b^q + b^{2q}}{3}\right)^{1/q}, \quad \text{where} \quad q = 1.6075. \tag{10}$$

Fig. 10 shows the results obtained by these models on a data set consisting of 5000 observations. The data are generated by the proposed model from uniform distributions over the intervals listed in Table 3. Table 4 shows the adjusted coefficients of determination $\bar{R}^2$ given by the exact Olkin-Pratt estimator (Karch [48]).

In fact, Fig. 10 and Table 4 clearly show that both solidity and sphericity can be predicted relatively reliably from the model parameters, with a coefficient of determination $\bar{R}^2$ greater than 0.9 in both cases. It should also be noted that in both cases the texture-related parameters (ℓ_T and c_T) are the most influential. In contrast, the results for normalized volume and surface area are more mixed, with lower $\bar{R}^2$ coefficients of determination of 0.74 and 0.86, respectively.

In general, the shape and angularity characteristics, which are otherwise dimensionless, are easier to predict. This is partly due to their low variance as a function of the model parameters, as shown in Figs. 8 and 9. Size characteristics, on the other hand, are more difficult to predict accurately, not only because of their higher variance, but also because they depend more on the ℓ_A and c_A parameters. For example, in the case of the volume, while it is true that perturbations due to a zero-mean Gaussian random field are partially compensated when the chord length is small, as is the case for G_T, which depends on c_T, this is no longer true when the chord length is of the order of the mesh, as is the case for the G_A field, which depends on ℓ_A.

3.3.4. Discussion

The proposed model aims to generate granular objects that can resemble compact aggregates of latex nanoparticles and offers a good compromise between flexibility and performance. Indeed, the use of a reduced number of parameters could lead one to believe that the model is not flexible enough. However, the results developed in the previous sections show strong correlations between the model parameters and the morphological characteristics of the generated objects, demonstrating a high degree of flexibility, as shown in Fig. 4.

In terms of performance, the generation of 1000 objects from two 3D random fields discretized on a 50^3 px grid and the mesh of a sphere composed of 10^4 faces takes about 20 s on a machine equipped with an Intel(R) Core(TM) i9-12900KF processor at 3.19 GHz and 64 GB of RAM; this time decreases to 4.5 s when the object generation is parallelized.

Furthermore, the SPHERE model allows the generation of compact random objects with controlled geometry using a limited number of parameters, thus avoiding classical problems such as the simplification of the shapes used to represent the objects (Han et al. [49]) or the inflation of the number of parameters, which leads to the curse of dimensionality, especially during optimization processes, as with models based on spherical harmonics (Garboczi and Bullard [25], Wei et al. [26] and Ueda [27]).

However, the proposed model is not limited to modeling compact nanoparticle aggregates and can be used to model larger granular objects such as rocks or coarse aggregates, as shown in the next section, and it is also possible to increase the level of detail by adding one or more Gaussian random fields, each of which adds two parameters to the model. On the other hand, the proposed model is not suitable for modeling non-compact objects such as soot or aerosol particle aggregates (Patiño et al. [11] and Kelesidis and Pratsinis [50]), sometimes referred to as fractal aggregates (Yazicioglu et al. [51]).

Finally, although the model itself depends on only 6 parameters, choices have to be made regarding the 3 meta-parameters, namely the number of vertices in the mesh (set to 10 200) and the grid sizes n_A and n_T used to generate the Gaussian fields G_A and G_T, both set to 50^3 px^3. The number of vertices allows the mesh to be fine enough to ensure that the difference between the volume of a sphere modeled in this way and the theoretical value is less than 0.1%, which is negligible for this particular application. See the Appendix for more information on the influence of mesh type vs. vertex count. The grid sizes n_A and n_T were chosen empirically to keep the model fast, while allowing the chord lengths ℓ_A and ℓ_T to be chosen over sufficiently large intervals for the application considered. To model finer details and thus smaller chord lengths, e.g. for G_T, it would be necessary to increase the corresponding grid sizes accordingly.

3.3.5. Generalization of model

As mentioned in the previous section, the model can be extended to make it even more flexible and realistic, even if this means increasing the number of parameters. This can be done in particular by adding Gaussian random fields of different chord lengths and intensities, each of these additions de facto adding two parameters to the model.

This extension of the model may prove useful in contexts other than this one, such as modeling granular objects more finely, or building a database of realistic granular 3D objects that can be compared to real data (Zhao et al. [52]) or used as a training set for machine learning applications. Fig. 11 shows some examples of objects generated by an extension of the model with 4 Gaussian random fields for a total of 10 parameters.

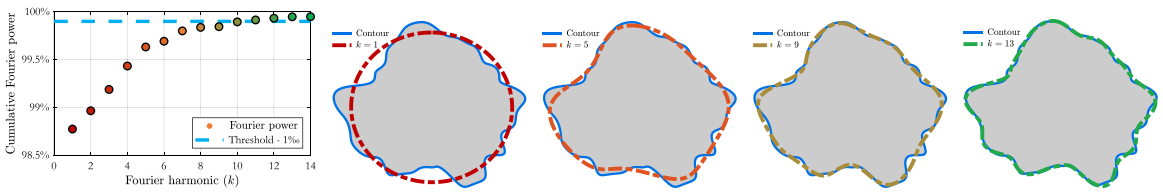

(a) Cumulative Fourier power (b) $k = 1$ (c) $k = 5$ (d) $k = 9$ (e) $k = 13$

Fig. 12. Evolution of the cumulative Fourier power as a function of the number of harmonics 12(a) and contour reconstruction as the number of harmonics increases.

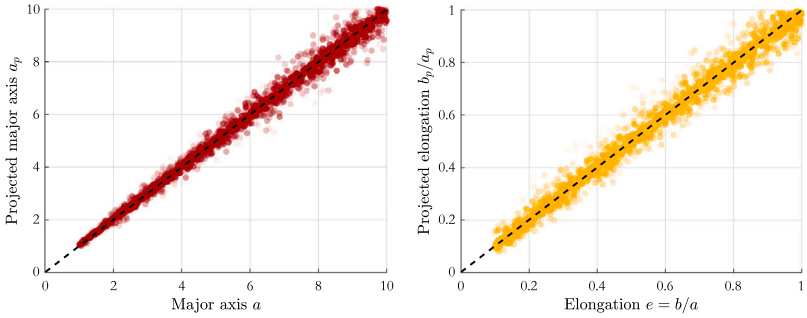

(a) Major axis – a **(b)** Elongation – e

Fig. 13. Illustration of the correlation between the elongation b/a and the projected elongation b_p/a_p on the one hand, and between the major axis a and the projected major axis a_p on the other hand. The data set consists of 5000 objects generated from the parameters of the Table 3 with $c_A < 0.3$.

4. Optimization and validation

The objective of this work is to model a population of latex nanoparticle aggregates using the proposed model. Real data are collected on 2D images from a morphogranulometer, and the idea is to optimize the model parameters by minimizing a cost function constructed from relative errors made on 2D characteristics.

The following sections aim to detail this method, starting with the optimization process, which is then validated on real data, namely 3D printed aggregates, and on a population of synthetic objects generated by the proposed model. Finally, the method is applied to images of latex nanoparticle aggregates and the results are presented and discussed.

4.1. Optimization process

4.1.1. Estimation based on direct measurements

The optimization process consists in defining a cost function to be minimized in order to find the optimal set of parameters for matching the morphological characteristics of the objects generated by the model with the observed data. However, some model parameters can be estimated directly from morphological properties measured directly on projected images of real objects, assuming that the objects are observed in an arbitrary direction orthogonal to that of the maximum Feret diameter, which is the case in the context of this article. This is particularly true for the major axis a and the elongation e, which can be used to estimate the minor axis b.

As mentioned in previous sections, the projected major axis, the projected minor axis, and the projected elongation are measured on the equivalent ellipse of the 2D projection of a 3D object along an arbitrary direction orthogonal to the maximum Feret diameter (see Fig. 6). These projected characteristics can be measured on 2D images of real objects and used to estimate the model parameters a and b. Indeed, there is a strong correlation between the projected major axis a_p and the major axis a, with an adjusted coefficient of determination $\bar{R}^2 = 0.988$, on the one hand (Fig. 13(a)), and between the projected elongation e_p and the elongation $e = b/a$, with an adjusted coefficient of determination $\bar{R}^2 = 0.977$, on the other hand (Fig. 13(b)), and the product of $a_p \times e_p$ can be used to estimate the minor axis b.

4.1.2. Definition of the cost function

The cost function must find an optimal set of parameters for the proposed model in order to best match the properties of the objects generated by the model with those measured on real data. Since the real data that are the object of study in this paper are 2D images of latex nanoparticle aggregates from a morphogranulometer, the assumption that the objects are projected along a direction orthogonal to the maximum Feret diameter is reasonable, and the measured properties are 2D morphological characteristics. Furthermore, two of the 6 model parameters, the major axis a and the minor axis b of the basic shape, can be estimated as explained in the previous section. The cost function $F_{\text{cost}}(\omega)$ is then defined as follows:

$$F_{\text{cost}}(\omega) = \Delta(A) + \Delta(A_k) + \Delta(P) + 2\Delta(\text{AR}) + \Delta(A_c) + \Delta(A_{c,k}) + \Delta(P_k) + \Delta(a_p) \tag{11}$$

where Δ is the relative error, A is the projected area, A_c is the convex area, P is the perimeter, a_p is the projected major axis, AR is the aspect ratio, X_k is the morphological characteristic X measured on the projected shape reconstructed from k elliptic Fourier descriptors (Kuhl and Giardina [31] and Crampton [32]), and $\omega = \{\ell_A, \ell_T, c_A, c_T\}$ is a subset of 4 parameters of the proposed model.

In fact, to take into account both the influence of the random field of angularity G_A and the random field of texture G_T on the projected measurements of area and perimeter, a simplified form of the 2D projection is used, reconstructed from a limited number k of harmonics of elliptic Fourier descriptors. The comparison of these two simplified contours should thus escape the influence of the parameters ℓ_T and c_T. The choice of the number k of harmonics used is therefore crucial and is decided on the basis of the concept of the *Fourier power* (Costa et al. [53]), which allows to quantify the deviation of the reconstruction of a contour from the original as a function of the number of harmonics used.

In practice, the Fourier power of the kth harmonic is defined as follows

$$\text{Fourier power} = \frac{a_k^2 + b_k^2 + c_k^2 + d_k^2}{2} \tag{12}$$

where a_k, b_k, c_k, and d_k are the Fourier coefficients associated with the projections of the contour along the x and y axes, respectively.

(a) STL geometry data for 3D printing (b) 2D projected image (c) Binarized image (d) 2D projected image of a synthetic aggregate (e) Synthetic aggregate

Fig. 14. Illustration of the process of generating real data from calibrated 3D printed aggregates by generating images using a morphogranulometer, and comparison with a synthetic aggregate generated by the proposed model.

Table 5
Comparison between 2D and 3D characteristics of 3D printed aggregates (ground truth) and synthetic aggregates generated by the proposed model with the optimal set of parameters. The values shown for synthetic aggregates are averages calculated from a set of 2048 aggregates. Values are rounded to the nearest two decimal places.

Characteristics	2D						3D					
	A (mm^2)	A_c (mm^2)	P (mm)	AR	Co	C	V (mm^3)	V_c (mm^3)	S (mm^2)	ESD (mm)	SLD	Φ_S
Ground truth	2.73	2.86	6.75	0.71	0.95	0.75	2.34	2.76	11.25	1.65	0.84	0.66
SPHERE model	2.72	2.81	6.80	0.71	0.96	0.74	2.34	2.83	11.25	1.65	0.83	0.66
Relative error (%)	0.24%	1.74%	0.76%	0.66%	1.40%	1.82%	0.19%	2.80%	0.06%	0.05%	2.47%	0.19%

By calculating the cumulative Fourier power for all harmonics up to a rank n corresponding to the Nyquist frequency (Crampton [32]), it is possible to set a threshold to determine the rank of the harmonic k to be used to reconstruct the simplified form. In practice, in the context of this work, the threshold is set to 99.9%. Fig. 12 illustrates the process of reconstructing a closed contour from an increasing number of harmonics, and Fig. 12(a) shows that the contour can be reconstructed with a cumulative Fourier power at the threshold of 99.9% from a number of harmonics $k = 10$.

The cost function F_{cost} thus defined by Eq. (11) can be optimized using a Particle Swarm Optimization (PSO) algorithm (Kennedy and Eberhart [54]) to fit the model parameters to the real data. Therefore, for each subset of parameters ω, a set of 1024 synthetic aggregates is generated using the proposed model. Their 2D projected morphological characteristics are measured and the mean values are used to calculate the relative errors with the real characteristics used by the cost function.

4.2. Validation on 3D printed aggregates

This section validates the optimization process and method for estimating the 3D characteristics of a granular object from the projected 2D characteristics. For this purpose, aggregates of about 2 millimeters in length are produced by additive 3D printing from a reference STL file representing a blackberry (Fig. 14(a)), whose shape is similar to the latex nanoparticle aggregates studied in this paper. Thus, the 3D properties of these 3D-printed aggregates are fully known, except for the approximations inherent in the printing process. Projected 2D images of the 3D printed aggregates are then acquired using a morphogranulometer (Morphologi G3 – Malvern Panalytical) (Fig. 14(b)), and the measurements made on these images, once binarized (Fig. 14(c)), constitute the real data set used to adjust the model parameters.

The model parameters are adjusted by performing measurements on the binary images, in particular, the major axis a and the minor axis b are estimated as explained in the previous section, and the other four parameters are estimated by PSO of the cost function F_{cost}. An optimal set of parameters is obtained, allowing the generation of aggregates using the proposed model (Fig. 14(e)), whose 2D characteristics match those of the real images (Fig. 14(d)) and whose 3D characteristics are also known. Note that in the context of this work, it is still assumed that the objects observed by the morphogranulometer are oriented in a direction orthogonal to the maximum Feret diameter.

To validate the method quantitatively, a set of 2048 synthetic aggregates is generated from the optimal set of parameters obtained at the end of the optimization process. The average values obtained for 2D and 3D morphological characteristics are calculated and compared with the 2D measurements made on real images from the morphogranulometer (Fig. 14(c)) and with the 3D characteristics from the reference STL file (Fig. 14(a)). The results are shown in Table 5. Overall, in terms of both 2D projections and 3D geometry, the properties of the objects generated by the model are very close to those of the calibrated 3D printed aggregates.

A comparison of the results obtained using the proposed model with those of other models based on hard sphere packing used on the same real dataset (Théodon et al. [13,55]), the proposed model consistently produces overall results closer to the ground truth, and with a much shorter computation time (a few hundredths of a second compared with several tenths of a second to generate an object). Furthermore, previous models not only required the same hypothesis of observing the object in a direction orthogonal to the maximum Feret diameter, but also imposed assumptions about the volume, convexity, and symmetry of the object that the model proposed in this paper does not require. As a result, the proposed method for retrieving 3D information from 2D measurements using the model and optimization process described in the previous sections is not only validated, but also shown to be more efficient as it is more robust and faster than previously proposed methods based on hard sphere packing models.

4.3. Validation on a population of synthetic objects

In the previous section, the proposed method is validated on a single real aggregate. However, the object of study in this article is a population of several thousand latex nanoparticle aggregates. Therefore, it is not feasible to apply an optimization process to each individual object, and it may be of interest to extend the method to the entire population of aggregates. In this section, the extension of the method to a population of granular objects is investigated.

To create a data set, the SPHERE model generates a sample of 250,000 objects from a set of parameters Ω_s consisting of random variables defined as follows:

$$\Omega_s = \{a_s, b_s, \ell_{A,s}, \ell_{T,s}, c_{A,s}, c_{T,s}\} \tag{13}$$

where

$$a_s \sim \text{LogNormal}(\mu_s, \sigma_s^2),\ \mu_s = \log(0.5) \text{ and } \sigma = 0.3 \tag{14}$$

$$b_s \sim a_s \times \text{Beta}(\alpha_s, \beta_s),\ \alpha_s = 10 + 0.5 \times a_s \text{ and } \beta_s = 1 \tag{15}$$

$$c_{T,s} \sim \left|\mathcal{N}(0.1, 0.01^2)\right| \tag{16}$$

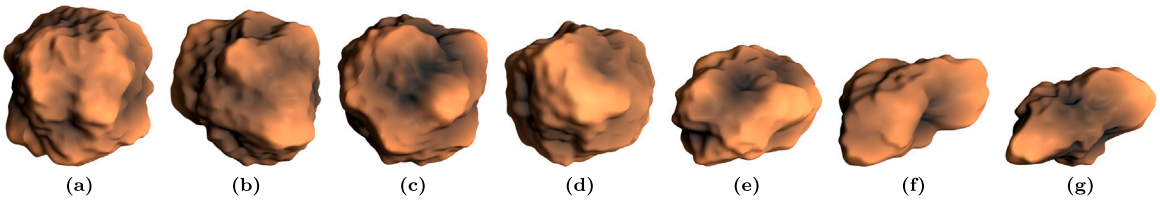

Fig. 15. Example of objects generated by the SPHERE model from the set of parameters Ω_s that make up the sample of 250,000 objects used for the numerical validation of the optimization method.

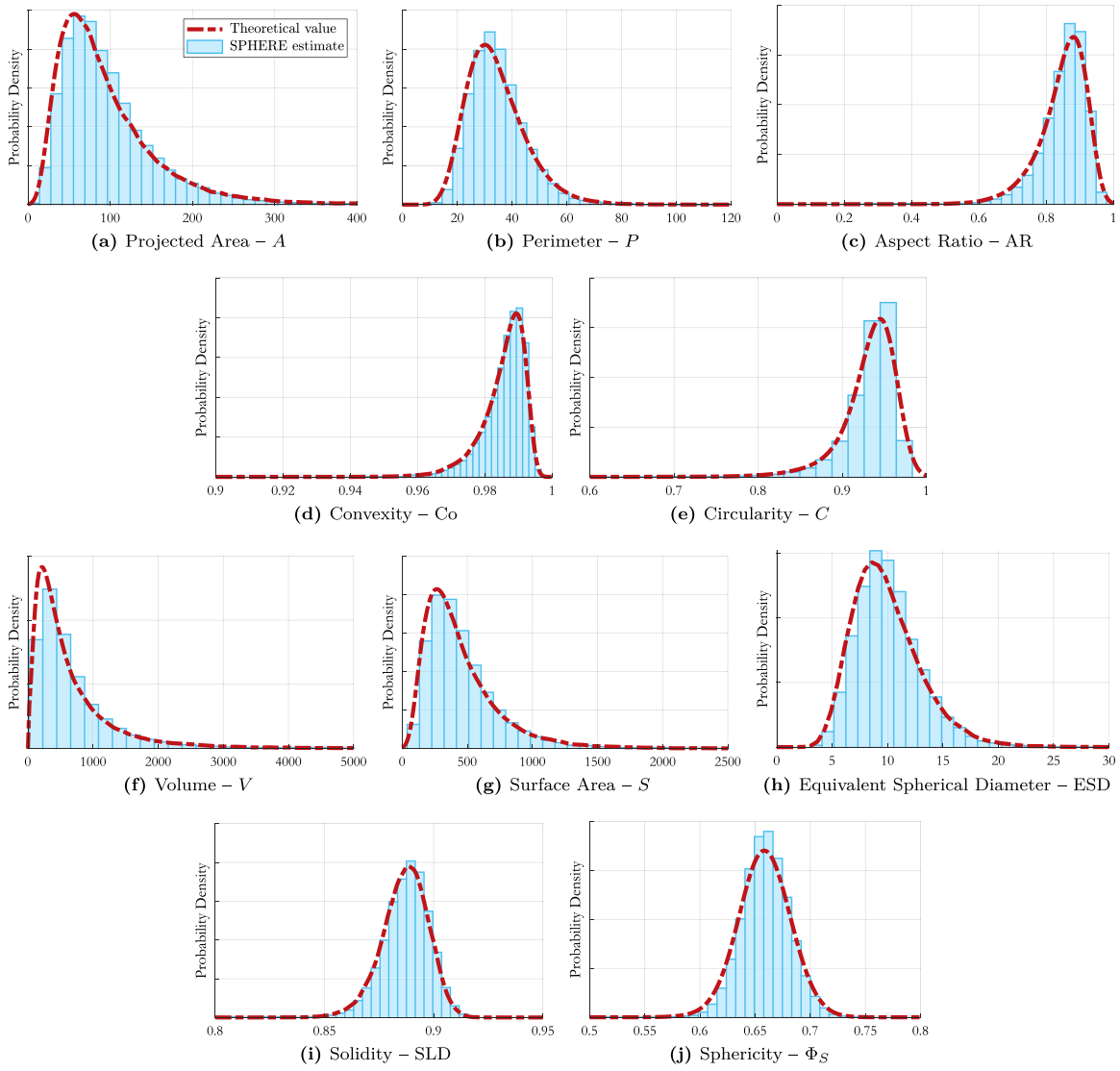

Fig. 16. Illustration of the results obtained by numerical validation of the proposed method. The dashed red lines represent the kernel probability densities estimated on the sample of 250,000 objects generated by the SPHERE model from the set of parameters Ω_s. The histograms represent the morphological characteristics of the population generated by the SPHERE model from the set of parameters $\hat{\Omega}_s$ estimated by the proposed optimization method.

Table 6
Comparison between the mean values of the morphological characteristics of the sample of 250,000 objects generated by the SPHERE model using the set of parameters Ω_s and the mean values of the morphological characteristics of the objects generated by the SPHERE model using the optimal parameterization $\hat{\Omega}_s$ obtained by the proposed optimization method. Values are rounded to the nearest two decimal places.

Characteristics	2D						3D					
	A (px^2)	A_c (px^2)	P (px)	AR	Co	C	V (px^3)	V_c (px^3)	S (px^2)	ESD (px)	SLD	Φ_S
Original sample	95.7	96.8	34.3	0.85	0.99	0.93	680	765	449	9.93	0.88	0.66
SPHERE model	96.4	97.4	34.6	0.87	0.99	0.94	713	809	462	10.4	0.88	0.67
Relative error (%)	0.7%	0.6%	0.8%	1.9%	0.1%	0.7%	4.9%	5.8%	3.1%	4.3%	0.3%	1.1%

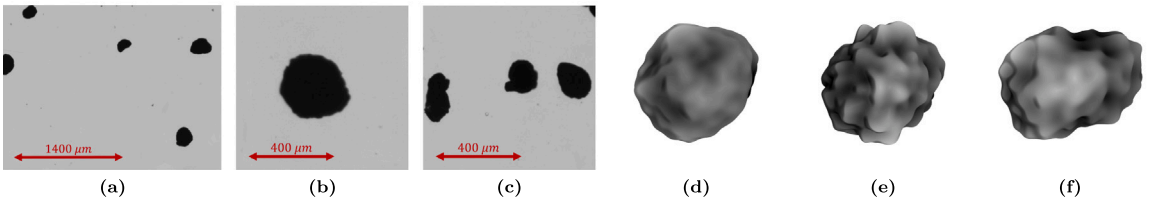

Fig. 17. Left: Illustrations of 2D projections taken by the morphogranulometer. Right: Example of 3D objects generated by the SPHERE model after the optimization process with the optimal set of parameters.

Table 7
Parameters used to generate the population of 250,000 random objects using the SPHERE model.

Parameter	$\ell_{A,s}$	$c_{A,s}$	$\ell_{T,s}$
Value	15	0.25	2

and other parameters are listed in Table 7.

The population is thus generated from two joint probability distributions for the principal axes of the ellipsoid, which forms the basic shape of the SPHERE model, and a normal distribution for the intensity of the texture random field G_C. This ensures a correlation between the morphological properties of the generated objects. Once the sample of 250,000 random objects has been generated (Fig. 15), the method described in the previous sections is used again to obtain an estimate of the model parameters.

The estimators $\hat{a}_s$ and $\hat{b}_s$ are two joint density probabilities, obtained from the kernel probability distributions f_{a_p} and $a_p \times f_{e_p}$, calculated from the histograms of the projected major axes a_p and the projected elongations $e_p = b_p/a_p$ of the equivalent projected ellipses. The other four parameters are then estimated by applying the PSO to the optimization function F_{cost}, the latter being redefined based on the relative errors to the mean values of the morphological characteristics considered. The result is an optimal parameterization $\hat{\Omega}_s$, which has the following definition:

$$\hat{\Omega}_s = \{\hat{a}_s, \hat{b}_s, \hat{\ell}_{A,s}, \hat{\ell}_{T,s}, \hat{c}_{A,s}, \hat{c}_{T,s}\} \tag{17}$$

where $\hat{x}$ is the estimated parameter x and $\hat{a}_s$ and $\hat{b}_s$ are two random variables.

Table 6 shows the deviations between the mean values of the two populations, the sample of 250,000 objects on the one hand, and a population of 10,000 objects generated by the SPHERE model using the optimal parameterization $\hat{\Omega}_s$ on the other, and Fig. 16 shows the deviations between the probability densities of the morphological characteristics of these two populations. The results obtained tend to validate the method, with relative errors on the mean values all below 6% and estimated probability densities in agreement with theoretical data. In other words, the proposed method for estimating model parameters from measurements of morphological characteristics on 2D projections of a population of 3D objects, and in particular by using an optimization process, seems to make it possible to determine a model parameterization with which a population of objects representative of the initial population can be generated in order to estimate its 3D morphological characteristics. In the next section, the method is applied to a dataset consisting of images of latex nanoparticle aggregates captured by a morphogranulometer, with the aim of estimating the 3D morphological characteristics of the aggregates.

5. Application: Latex nanoparticle aggregates

In this section, the method for estimating the 3D characteristics of a population of granular objects from 2D projections along a direction orthogonal to the maximum Feret diameter is applied to a population of latex nanoparticle aggregates.

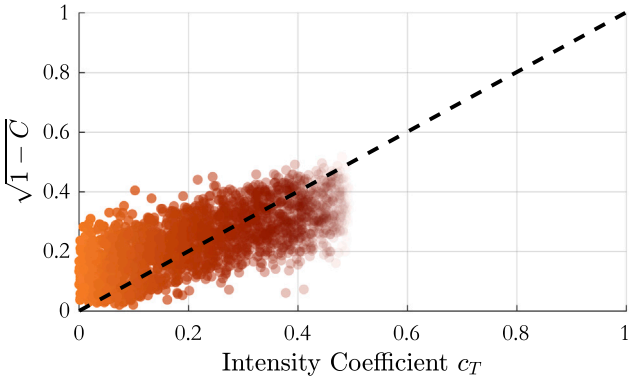

Fig. 18. Illustration of the correlation between the intensity coefficient c_T of the random field of texture G_T and the circularity C. The data was generated by the SPHERE model using the parameters in Table 3 with $c_T < 50\%$.

5.1. Methodology

A set of 3500 images is captured by a morphogranulometer (Morphologi G3 – Malvern Panalytical), within which just over 5000 aggregates are identified (Fig. 17). The aggregates have an average size (ECD) of about 250 μm, with the smallest measuring a few tens of microns and the largest a few hundred microns (Fig. 19(f)). The images are cleaned and binarized, and projected 2D measurements are made (Hamieh et al. [33]). The method described in the previous sections is then applied. An optimal parameterization $\hat{\Omega}_r$ for the SPHERE model is estimated from measurements made on real images.

$$\hat{\Omega}_r = \{\hat{a}_r, \hat{b}_r, \hat{\ell}_{A,r}, \hat{\ell}_{T,r}, \hat{c}_{A,r}, \hat{c}_{T,r}\} \tag{18}$$

where $\hat{a}_r$ and $\hat{b}_r$ are random variables estimated from the distributions of the projected major axes and projected elongations of equivalent projected ellipses. However, unlike the previous protocol, where the intensity coefficient c_T of the random field of texture G_T was a scalar, the non-negligible correlation between the circularity C and the intensity coefficient c_T is taken into account to estimate the latter more finely.

In fact, Fig. 18 shows that there is some correlation between the intensity coefficient c_T on the one hand and the quantity $\sqrt{1-C}$ on the other, with an adjusted coefficient of determination $\bar{R}^2 > 0.5$. Consequently, the estimator of the intensity coefficient $\hat{c}_{T,r}$ is a random variable written as follows:

$$\hat{c}_{T,r} = \alpha_0 + \alpha_1 \sqrt{1-C} + \varepsilon \tag{19}$$

The three parameters $\hat{a}_r$, $\hat{b}_r$ and $\hat{c}_{T,r}$ are therefore random variables that depend on the three joint probability density functions f_{a_p}, f_{e_p} and f_C estimated by the 2D morphological characteristic measurements made on the morphogranulometer images.

This estimate of the intensity coefficient c_T makes it possible to include objects whose circularity is very close to 1, which is impossible if c_T is a scalar, as shown in Figs. 8(f) and 9(f). The remaining three parameters are then estimated by optimizing the cost function F_{cost} using the PSO algorithm.

Table 8
Comparison of the mean values of 2D morphological characteristics measured on real images and on the population of 10,000 granular objects generated by the SPHERE model using the optimal parameterization $\widehat{\Omega}_r$. The mean values of the 3D morphological characteristics of synthetic objects are also shown. Values are rounded to the nearest two decimal places.

Characteristics	2D						3D					
	A (µm^2)	A_c (µm^2)	P (µm)	AR	Co	C	V (µm^3)	V_c (µm^3)	S (µm^2)	ESD (µm)	SLD	Φ_S
Ground truth	5.3×10^4	5.6×10^4	890	0.73	0.94	0.79	–	–	–	–	–	–
SPHERE model	5.3×10^4	5.7×10^4	893	0.74	0.93	0.77	7.1×10^6	9.4×10^6	2.2×10^5	220	0.78	0.68
Relative error (%)	0%	0.8%	0.3%	0.4%	0.8%	3.1%	–	–	–	–	–	–

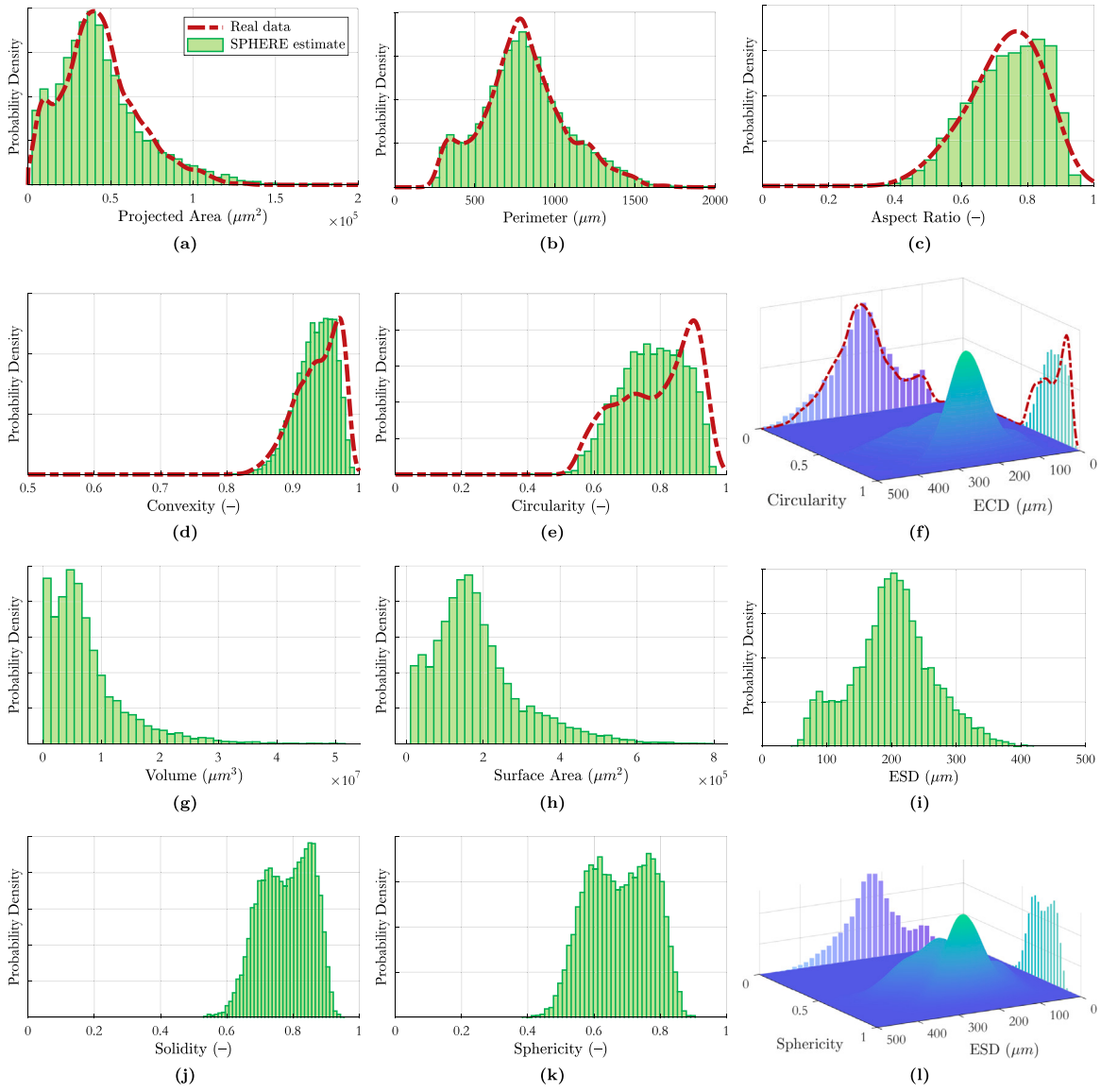

Fig. 19. Illustration of the results obtained by the proposed method on real data. The dashed red lines represent the kernel probability densities estimated from real data measured on projected 2D images of latex nanoparticle aggregates. The histograms in green represent the 2D and 3D morphological characteristics of the aggregate population generated by the SPHERE model using the optimal set of parameters $\widehat{\Omega}_r$. (For interpretation of the references to color in this figure legend, the reader is referred to the web version of this article.)

5.2. Results & discussion

A population of 10,000 synthetic granular objects is generated by the SPHERE model using the optimal parameterization $\widehat{\Omega}_r$, as shown in Fig. 17, and 2D and 3D measurements are performed. Table 8 shows the results obtained and the relative errors made on the averages of 2D morphological characteristics measured on real data, on the one hand, and on synthetic objects, on the other hand. Fig. 19 shows the probability density functions for the 2D and 3D size and shape characteristics of the synthetic objects, allowing comparison of the results obtained with the 2D morphological characteristics measured on the real images from the morphogranulometer.

In particular, relative errors on 2D morphological characteristics are very low, with excellent approximation of projected area and perimeter distributions. The aspect ratio and convexity are also quite well approximated. Only the measured and estimated circularity distributions show a clear difference. As a first approximation, the estimated intensity coefficient $\widehat{c}_{T,r}$ was a scalar, and this difference was even more pronounced.

This discrepancy between the measured and theoretical distributions can therefore be partly explained by a non-optimal estimation of the parameters influencing the circularity, namely $\hat{c}_{T,r}$, but also $\hat{c}_{A,r}$, which is still a scalar in the current model.

An important aspect of the proposed method is the consideration of correlations between different morphological characteristics, as illustrated in Figs. 19(f) and 19(l), where the joint probability densities and marginal densities of circularity and ECD on the one hand, in the 2D case, and sphericity and ESD on the other hand, in the 3D case, are shown. In fact, it appears that smaller objects tend to be more circular (or spherical), such that the elongation, circularity, and sphericity tend to approach 1 as size (ECD or ESD) decreases. These results are also consistent with previous work (Hamieh et al. [33]) where the 2D characteristics were measured by image analysis and the 3D size characteristics (ESD) were measured by laser diffraction.

Overall, the results obtained for the estimation of the distributions of the 2D morphological characteristics are comparable to those of the numerical validation of the method. Thus, the 2D agreement and the agreement of the results with previous work on the same dataset tend to validate the estimation of the main 3D morphological characteristics of the aggregates studied, under the assumption that the objects are indeed observed along a direction orthogonal to the maximum Feret diameter.

6. Strengths, limitations & prospects

6.1. Strengths

As mentioned in the first section, the strengths and originality of the proposed approach can be summarized in three points.

1. The SPHERE model presented in Section 3 allows the efficient generation of granular objects with complex morphology, as shown qualitatively in Figs. 4 and 11, and as demonstrated by the results obtained when modeling real data, with deviations of less than 5% on average.
2. The SPHERE model, which uses 3D Gaussian fields, is independent of the underlying mesh. This also allows a high degree of flexibility while limiting the number of model parameters. The FFT-based algorithm for generating the Gaussian random fields provides very good performance. It also allows the optimization process to be applied to a population of objects.
3. The optimization process, based on a multi-scale approach with partial contour reconstruction using Fourier descriptors, is validated on real 3D printed data and on a population of synthetic objects, with very good results in both cases.

The SPHERE model is therefore a fast and efficient way to generate star-shaped objects with great flexibility and relatively good control over their morphology (more than 1000 objects in only 5 s). The use of 3D fields makes the method completely independent of the mesh used and can be adapted to any star-shaped object. In addition, the SPHERE model can be easily extended and made more flexible by using more than just two random fields, with each field adding two parameters to the model, as shown in Section 3.3.5.

Finally, the ability of the model to generate granular objects with controlled morphological properties extremely quickly may make it useful in other areas, such as Discrete Element Method (DEM) simulations of granular media (Cundall and Strack [56]), where circular or spherical shapes are often used for simplicity.

6.2. Limitations & prospects

The results presented in the previous section, put into perspective by the results obtained through the validation process with 3D printed aggregates on the one hand and synthetic aggregates on the other, tend to validate the proposed method. In fact, the distributions of the 2D size characteristics (area, perimeter, ECD) proposed by the model are in excellent agreement with what can be measured on the morphogranulometer images. As for the 2D shape and angularity characteristics, aspect ratio and convexity are estimated quite well, with only circularity showing a slight offset. Therefore, although the ground truth is unknown, it can be assumed that the estimation of the 3D characteristic distributions is a first result, not perfect, but certainly no less relevant. There are a number of reasons for these results, which may be limitations of the model itself, but also prospects for future work.

1. In the current model, three of the six parameters are scalars that are fixed in advance, but the use of random variables that depend on probability density functions, possibly correlated with other model parameters, as in the case of the intensity coefficient c_T of the random field G_T, could perhaps provide more realistic results.
2. As it stands, the number of model parameters is set to six, since only two random fields are used. It is conceivable that a model with more than two random fields could be used, with each field requiring the addition of two parameters. A balance would then have to be struck between the number of parameters and the flexibility of the model, especially since adding parameters can make it difficult to fit the data and account for subtle correlations.
3. Finally, it is possible that the assumption that aggregates are always observed in a direction orthogonal to the maximum Feret diameter is questionable. Ideally, this hypothesis should be discarded, which would also make it possible to work with ex situ images of the reactor in which the latex nanoparticle aggregation process takes place, where no hypothesis can be made about the direction in which the aggregates are observed.

Nevertheless, the validation process, and in particular the validation on 3D printed aggregates, showed the effectiveness of the method for aggregates with relative cylindrical symmetry, improving on the results previously obtained with overlapping sphere models (Théodon et al. [13,55]).

In a future work, the method will be enriched and applied to ex-situ images of latex nanoparticle aggregates observed in arbitrary directions, making it necessary to abandon the assumption of observing objects along a privileged direction. In addition, it would also be interesting to build a multi-scale agglomeration model, where granular objects generated by the SPHRE model presented in this article would then be agglomerated to better represent reality. To this end, previous models developed based on hard sphere packing could be adapted to use the granular objects generated by the SPHRE model as building blocks.

7. Conclusion

The SPHERE (Stochastic Process for Highly Effective Radial Expansion) model, as described in this paper, proposes an original approach to the geometric modeling of granular objects. Its ability to manipulate an ellipsoid mesh with 3D Gaussian random fields has proven effective in controlling both 2D and 3D morphological properties of granular objects, demonstrating its flexibility and speed. Validated by comparison with real and synthetic objects, the model demonstrates accuracy in reproducing the shape, angularity and texture of aggregates, with relative errors below 6%.

This model is notable for its independence from mesh type and its computational efficiency, generating over a thousand aggregates in a few seconds. While efficient in its current form, the model is primarily suited to star-shaped objects, suggesting potential areas for future exploration and extension. The results and methodology presented in this study can be used as a basis for future applications and enhancements in various scientific and industrial fields where accurate morphological characterization of granular materials is critical.

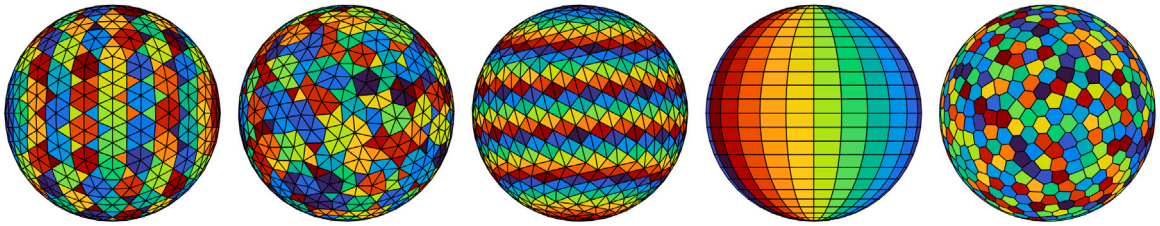

(a) Icosphere (b) Thomson (c) Fibonacci (d) Rectangle (e) Voronoi

Fig. 20. Illustration of five different types of spherical meshes with a total of 642 vertices.

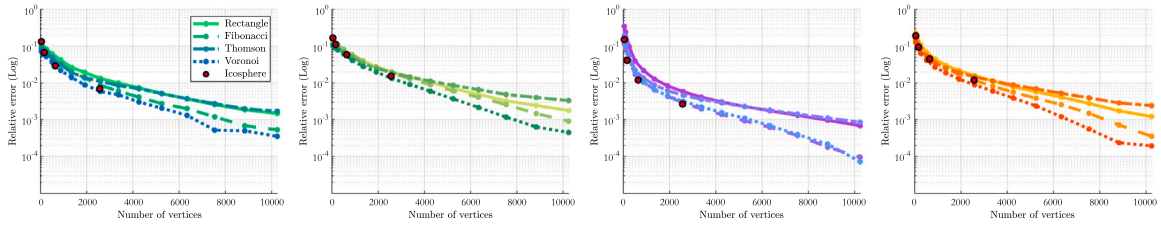

(a) Solidity – SLD (b) Sphericity – Φ_S (c) Volume – V (d) Surface Area – S

Fig. 21. Illustration of the relative difference between measurements made on objects generated with the SPHERE model from five different meshes. Reference measurements are made on an icosphere with 10,242 vertices.

CRediT authorship contribution statement

L. Théodon: Conceptualization, Methodology, Software, Validation, Visualization, Writing – original draft, Writing – review & editing. **C. Coufort-Saudejaud:** Supervision, Writing – review & editing. **J. Debayle:** Supervision, Writing – review & editing.

Declaration of competing interest

None

Data availability

Data will be made available on request.

Acknowledgment

The author(s) acknowledge(s) the support of the French Agence Nationale de la Recherche (ANR), under grant ANR-20-CE07-0025 (MORPHING project).

Additional resources

The MATLAB® (2023b) code for the SPHERE model is available in a GitHub repository at: https://github.com/ltheodon/SPHERE.

The STL files used to design the 3D printed aggregates are available for purchase on CGTrader at: https://www.cgtrader.com/3d-models/food/fruit/blackberry-001.

Appendix. Mesh comparison

Deforming the mesh of a sphere from a random field can be difficult to implement. Traditional techniques use spherical noise (e.g., Perlin or Simplex) or random fields that must satisfy periodicity conditions. For all these reasons, using an arbitrary mesh can sometimes be challenging. For example, Mollon and Zhao [23] uses a geodesic mesh with 2562 vertices obtained by three successive subdivisions of an icosahedron. The mesh is then deformed by several 2D Gaussian random fields whose covariance matrices are all precomputed for different chord lengths. However, this method is not feasible for irregular or random meshes. In this appendix, five different meshes of a sphere are deformed from the SPHERE model and the relative errors for different morphological features are calculated, taking as reference measurements obtained for a mesh of 10,242 vertices of an icosphere.

A sphere can be meshed in different ways depending on the context and requirements. For example, some applications may require regular or uniform meshing. The five meshes being compared are defined as follows.

1. A geodesic mesh (here an icosphere) can be obtained by successive subdivisions of a regular polygon, in this case an icosahedron (Fig. 20(a)). For example, three subdivisions yield a mesh with 2562 vertices, and four subdivisions yield a mesh with 10,242 vertices. While this has the advantage of providing a uniform distribution of points on the sphere, it does not allow the selection of an appropriate number of vertices for a particular application (Kent [57]).
2. A Thomson configuration (T-design) proposes a uniform distribution of mesh vertices over the surface of the sphere (Fig. 20(b)). It can be obtained by *energy minimization* from an initial configuration by moving the vertices so that they are farthest apart. It can be computationally expensive, but the number of vertices is up to the user (Brauchart and Grabner [58]).
3. A mesh based on a Fibonacci grid (Fig. 20(c)) has the advantage of being extremely easy to implement, but the major drawback is the quasi-uniform distribution of points, which may not be suitable for certain applications (Keinert et al. [59]).
4. A rectangular or quadrilateral mesh is a classic subdivision of a sphere along meridian and parallel lines, and has the advantage of being very easy to implement (Fig. 20(d)). However, the distribution of the vertices is not uniform, with a high density at the poles, and the size of the faces is larger at the equator. This is the mesh used by the sphere function in MATLAB®.
5. A Voronoi mesh provides a uniform distribution of vertices on the surface of the sphere. The mesh can be obtained by successively applying the Loyd relaxation algorithm to any random distribution of points on the sphere (Du et al. [60]), or by iteratively adding new vertices (Augenbaum and Peskin [61]). In fact, generating this mesh with the assurance of a quasi-uniform spatial distribution of vertices can be computationally time-consuming.

Ten different objects are generated using the SPHERE model, each object using the five different types of meshes with the same number of vertices (except for geodesic meshes). Morphological characteristics of shape and size are measured and compared with values obtained from an icosphere mesh with 10,242 vertices. Fig. 21 shows that for a mesh of 10,000 vertices, the relative errors are less than 0.2%. Furthermore, the relative error curves are all very similar, confirming that the 3D random field deformation method is independent of the mesh used.

References

[1] Z.M. Lu, L. Zhang, D.M. Fan, N.M. Yao, C.X. Zhang, Crystal texture recognition system based on image analysis for the analysis of agglomerates, Chemometr. Intell. Lab. Syst. 200 (2020) 103985, http://dx.doi.org/10.1016/j.chemolab.2020.103985, URL https://www.sciencedirect.com/science/article/pii/S0169743919307695.

[2] A. Lowe, G. Singh, H.-K. Chan, A. Masri, S. Cheng, A. Kourmatzis, Fragmentation dynamics of single agglomerate-to-wall impaction, Powder Technol. 378 (2021) 561–575, http://dx.doi.org/10.1016/j.powtec.2020.10.021, URL https://www.sciencedirect.com/science/article/pii/S0032591020309645.

[3] R. Pashminehazar, S.J. Ahmed, A. Kharaghani, E. Tsotsas, Spatial morphology of maltodextrin agglomerates from X-ray microtomographic data: Real structure evaluation vs. spherical primary particle model, Powder Technol. 331 (2018) 204–217, http://dx.doi.org/10.1016/j.powtec.2018.03.008, URL https://www.sciencedirect.com/science/article/pii/S0032591018301918.

[4] I. Atalar, F. Yazici, Effect of different binders on reconstitution behaviors and physical, structural, and morphological properties of fluidized bed agglomerated yoghurt powder, Drying Technol. 37 (13) (2019) 1656–1664, http://dx.doi.org/10.1080/07373937.2018.1529038, arXiv:https://doi.org/10.1080/07373937.2018.1529038.

[5] P. Romphophak, C. Coufort-Saudejaud, C. Le Men, P. Painmanakul, A. Liné, Analysis of flocculation in a jet clarifier. Part 2 - Analysis of aggregate size distribution versus Camp number, Chem. Eng. Res. Des. 175 (2021) 392–402, http://dx.doi.org/10.1016/j.cherd.2021.09.008, URL https://www.sciencedirect.com/science/article/pii/S0263876221003683.

[6] O. Cohen, D. Michaels, Y. Yavor, Agglomeration in composite propellants containing different nano-aluminum powders, Propellants Explos. Pyrotech. 47 (9) (2022) e202100320, http://dx.doi.org/10.1002/prep.202100320, arXiv:https://onlinelibrary.wiley.com/doi/pdf/10.1002/prep.202100320 URL https://onlinelibrary.wiley.com/doi/abs/10.1002/prep.202100320.

[7] Z. Liu, C. Zhang, L. Shao, J. Wang, Study on quantitative characterization of morphological characteristics and high temperature performance evaluation of coarse aggregate based on computer vision, Front. Mater. 7 (2021) http://dx.doi.org/10.3389/fmats.2020.607105, URL https://www.frontiersin.org/articles/10.3389/fmats.2020.607105.

[8] M. Kamani, R. Ajalloeian, Investigation of the changes in aggregate morphology during different aggregate abrasion/degradation tests using image analysis, Constr. Build. Mater. 314 (2022) 125614, http://dx.doi.org/10.1016/j.conbuildmat.2021.125614, URL https://www.sciencedirect.com/science/article/pii/S0950061821033511.

[9] S. Murugadoss, F. Brassinne, N. Sebaihi, J. Petry, S.M. Cokic, K.L. Van Landuyt, L. Godderis, J. Mast, D. Lison, P.H. Hoet, S. van den Brule, Agglomeration of titanium dioxide nanoparticles increases toxicological responses in vitro and in vivo, Part. Fibre Toxicol. 17 (1) (2020) 10, http://dx.doi.org/10.1186/s12989-020-00341-7.

[10] D. Cortés, J. Morán, F. Liu, F. Escudero, J.-L. Consalvi, A. Fuentes, Effect of fuels and oxygen indices on the morphology of soot generated in laminar coflow diffusion flames, Energy Fuels 32 (11) (2018) 11802–11813, http://dx.doi.org/10.1021/acs.energyfuels.8b01301.

[11] F. Patiño, J. Cruz, I. Verdugo, J. Morán, J. Consalvi, F. Liu, X. Du, A. Fuentes, Soot primary particle sizing in a n-heptane doped methane/air laminar coflow diffusion flame by planar two-color TiRe-LII and TEM image analysis, Fuel 266 (2020) 117030, http://dx.doi.org/10.1016/j.fuel.2020.117030, URL https://www.sciencedirect.com/science/article/pii/S0016236120300259.

[12] Q. Wang, J. He, J. Sun, J. Ho, Determining the specific surface area of coarse aggregate based on sieving curve via image-analysis approach, Constr. Build. Mater. 305 (2021) 124728, http://dx.doi.org/10.1016/j.conbuildmat.2021.124728, URL https://www.sciencedirect.com/science/article/pii/S0950061821024831.

[13] L. Théodon, C. Coufort-Saudejaud, J. Debayle, GRAPE: A stochastic geometrical 3D model for aggregates of particles with tunable 2D morphological projected properties, Image Anal. Stereol. 42 (1) (2023) 1–16, http://dx.doi.org/10.5566/ias.2875, URL https://www.ias-iss.org/ojs/IAS/article/view/2875.

[14] M. Wozniak, F. Onofri, S. Barbosa, J. Yon, J. Mroczka, Comparison of methods to derive morphological parameters of multi-fractal samples of particle aggregates from TEM images, J. Aerosol Sci. 47 (2012) 12–26, http://dx.doi.org/10.1016/j.jaerosci.2011.12.008, URL https://www.sciencedirect.com/science/article/pii/S0021850211001984.

[15] E. Guesnet, R. Dendievel, D. Jauffrès, C. Martin, B. Yrieix, A growth model for the generation of particle aggregates with tunable fractal dimension, Physica A 513 (2019) 63–73, http://dx.doi.org/10.1016/j.physa.2018.07.061, URL https://www.sciencedirect.com/science/article/pii/S0378437118309336.

[16] J. Morán, A. Fuentes, F. Liu, J. Yon, FracVAL: An improved tunable algorithm of cluster–cluster aggregation for generation of fractal structures formed by polydisperse primary particles, Comput. Phys. Comm. 239 (2019) 225–237, http://dx.doi.org/10.1016/j.cpc.2019.01.015, URL https://www.sciencedirect.com/science/article/pii/S0010465519300323.

[17] O.V. Tomchuk, M.V. Avdeev, L.A. Bulavin, Modeling fractal aggregates of polydisperse particles with tunable dimension, Colloids Surf. A 605 (2020) 125331, http://dx.doi.org/10.1016/j.colsurfa.2020.125331, URL https://www.sciencedirect.com/science/article/pii/S0927775720309249.

[18] M. Moreaud, G. Ferri, S. Humbert, M. Digne, J.-M. Schweitzer, Simulation of large aggregate particles system with a new morphological model, Image Anal. Stereol. 40 (2) (2021) 71–84, http://dx.doi.org/10.5566/ias.2488, URL https://www.ias-iss.org/ojs/IAS/article/view/2488.

[19] J.-F. Ferellec, G.R. McDowell, A method to model realistic particle shape and inertia in DEM, Granul. Matter 12 (5) (2010) 459–467, http://dx.doi.org/10.1007/s10035-010-0205-8.

[20] G. Mollon, J. Zhao, Fourier–Voronoi-based generation of realistic samples for discrete modelling of granular materials, Granul. Matter 14 (5) (2012) 621–638, http://dx.doi.org/10.1007/s10035-012-0356-x.

[21] J. Chen, R. Li, P.-Q. Mo, G. Zhou, S. Cai, D. Chen, A modified method for morphology quantification and generation of 2D granular particles, Granul. Matter 24 (1) (2021) 16, http://dx.doi.org/10.1007/s10035-021-01149-8.

[22] G. Mollon, J. Zhao, Generating realistic 3D sand particles using Fourier descriptors, Granul. Matter 15 (1) (2013) 95–108, http://dx.doi.org/10.1007/s10035-012-0380-x.

[23] G. Mollon, J. Zhao, 3D generation of realistic granular samples based on random fields theory and Fourier shape descriptors, Comput. Methods Appl. Mech. Engrg. 279 (2014) 46–65, http://dx.doi.org/10.1016/j.cma.2014.06.022, URL https://www.sciencedirect.com/science/article/pii/S0045782514002084.

[24] A. Baxansky, N. Kiryati, Calculating geometric properties of three-dimensional objects from the spherical harmonic representation, Pattern Recognit. 40 (2) (2007) 756–770, http://dx.doi.org/10.1016/j.patcog.2006.06.001, URL https://www.sciencedirect.com/science/article/pii/S003132030600272X.

[25] E. Garboczi, J. Bullard, 3D analytical mathematical models of random star-shape particles via a combination of X-ray computed microtomography and spherical harmonic analysis, Adv. Powder Technol. 28 (2) (2017) 325–339, http://dx.doi.org/10.1016/j.apt.2016.10.014, URL https://www.sciencedirect.com/science/article/pii/S0921883116302953.

[26] D. Wei, J. Wang, B. Zhao, A simple method for particle shape generation with spherical harmonics, Powder Technol. 330 (2018) 284–291, http://dx.doi.org/10.1016/j.powtec.2018.02.006, URL https://www.sciencedirect.com/science/article/pii/S0032591018301189.

[27] T. Ueda, Particle shape generation using spherical harmonic modeling and principal component analysis and application of the discrete element method, J. Soc. Powder Technol. Jpn. 60 (3) (2023) 143–148, http://dx.doi.org/10.4164/sptj.60.143, URL https://cir.nii.ac.jp/crid/1390577441946904064.

[28] L. Chen, Curse of dimensionality, in: L. Liu, M.T. Özsu (Eds.), Encyclopedia of Database Systems, Springer US, Boston, MA, 2009, pp. 545–546, http://dx.doi.org/10.1007/978-0-387-39940-9_133.

[29] J.B. Spjut, A.E. Kensler, E.L. Brunvand, Hardware-accelerated gradient noise for graphics, in: Proceedings of the 19th ACM Great Lakes Symposium on VLSI, GLSVLSI '09, Association for Computing Machinery, New York, NY, USA, 2009, pp. 457–462, http://dx.doi.org/10.1145/1531542.1531647.

[30] G.J. Hettinga, R. van Beckhoven, JiříKosinka, Noisy gradient meshes: Augmenting gradient meshes with procedural noise, Graph. Models 103 (2019) 101024, http://dx.doi.org/10.1016/j.gmod.2019.101024, URL https://www.sciencedirect.com/science/article/pii/S1524070319300153.

[31] F.P. Kuhl, C.R. Giardina, Elliptic Fourier features of a closed contour, Comput. Graph. Image Process. 18 (3) (1982) 236–258, http://dx.doi.org/10.1016/0146-664X(82)90034-X, URL https://www.sciencedirect.com/science/article/pii/0146664X8290034X.

[32] J.S. Crampton, Elliptic Fourier shape analysis of fossil bivalves: some practical considerations, Lethaia 28 (2) (1995) 179–186, http://dx.doi.org/10.1111/j.1502-3931.1995.tb01611.x, arXiv:https://onlinelibrary.wiley.com/doi/pdf/10.1111/j.1502-3931.1995.tb01611.x URL https://onlinelibrary.wiley.com/doi/abs/10.1111/j.1502-3931.1995.tb01611.x.

[33] A. Hamieh, C. Coufort-Saudejaud, A. Couffin, A. Liné, C. Frances, Temperature influence on MBS latex aggregate morphology, Colloids Surf. A 676 (2023) 132139, http://dx.doi.org/10.1016/j.colsurfa.2023.132139, URL https://www.sciencedirect.com/science/article/pii/S0927775723012232.

[34] M. Frei, F. Kruis, Image-based size analysis of agglomerated and partially sintered particles via convolutional neural networks, Powder Technol. 360 (2020) 324–336, http://dx.doi.org/10.1016/j.powtec.2019.10.020, URL https://www.sciencedirect.com/science/article/pii/S003259101930854X.

[35] P. Monchot, L. Coquelin, K. Guerroudj, N. Feltin, A. Delvallée, L. Crouzier, N. Fischer, Deep learning based instance segmentation of titanium dioxide particles in the form of agglomerates in scanning electron microscopy, Nanomaterials 11 (4) (2021) http://dx.doi.org/10.3390/nano11040968, URL https://www.mdpi.com/2079-4991/11/4/968.

[36] B. Rühle, J.F. Krumrey, V.-D. Hodoroaba, Workflow towards automated segmentation of agglomerated, non-spherical particles from electron microscopy images using artificial neural networks, Sci. Rep. 11 (1) (2021) 4942, http://dx.doi.org/10.1038/s41598-021-84287-6.

[37] J. Lins, T. Harweg, F. Weichert, K. Wohlgemuth, Potential of deep learning methods for deep level particle characterization in crystallization, Appl. Sci. 12 (5) (2022) http://dx.doi.org/10.3390/app12052465, URL https://www.mdpi.com/2076-3417/12/5/2465.

[38] L. Théodon, J. Debayle, C. Coufort-Saudejaud, Morphological characterization of aggregates and agglomerates by image analysis: A systematic literature review, Powder Technol. 430 (2023) 119033, http://dx.doi.org/10.1016/j.powtec.2023.119033, URL https://www.sciencedirect.com/science/article/pii/S0032591023008161.

[39] L. Guérin, C. Coufort-Saudejaud, A. Liné, C. Frances, Dynamics of aggregate size and shape properties under sequenced flocculation in a turbulent Taylor-Couette reactor, J. Colloid Interface Sci. 491 (2017) 167–178, http://dx.doi.org/10.1016/j.jcis.2016.12.042, URL https://www.sciencedirect.com/science/article/pii/S0021979716310426.

[40] L. Guérin, C. Frances, A. Liné, C. Coufort-Saudejaud, Fractal dimensions and morphological characteristics of aggregates formed in different physico-chemical and mechanical flocculation environments, Colloids Surf. A 560 (2019) 213–222, http://dx.doi.org/10.1016/j.colsurfa.2018.10.017, URL https://www.sciencedirect.com/science/article/pii/S0927775718313153.

[41] M. Grum, A.G. Bors, 3D modeling of multiple-object scenes from sets of images, Pattern Recognit. 47 (1) (2014) 326–343, http://dx.doi.org/10.1016/j.patcog.2013.04.020, URL https://www.sciencedirect.com/science/article/pii/S0031320313002197.

[42] L. Kang, L. Wu, Y. Wei, S. Lao, Y.-H. Yang, Two-view underwater 3D reconstruction for cameras with unknown poses under flat refractive interfaces, Pattern Recognit. 69 (2017) 251–269, http://dx.doi.org/10.1016/j.patcog.2017.04.006, URL https://www.sciencedirect.com/science/article/pii/S0031320317301516.

[43] T. Yan, Z. Hu, Y. Qian, Z. Qiao, L. Zhang, 3D shape reconstruction from multifocus image fusion using a multidirectional modified Laplacian operator, Pattern Recognit. 98 (2020) 107065, http://dx.doi.org/10.1016/j.patcog.2019.107065, URL https://www.sciencedirect.com/science/article/pii/S003132031930367X.

[44] P. Adler, C. Jacquin, J. Quiblier, Flow in simulated porous media, Int. J. Multiph. Flow 16 (4) (1990) 691–712, http://dx.doi.org/10.1016/0301-9322(90)90025-E, URL https://www.sciencedirect.com/science/article/pii/030193229090025E.

[45] Z. Liang, C. Fernandes, F. Magnani, P. Philippi, A reconstruction technique for three-dimensional porous media using image analysis and Fourier transforms, J. Pet. Sci. Eng. 21 (3) (1998) 273–283, http://dx.doi.org/10.1016/S0920-4105(98)00077-1, URL https://www.sciencedirect.com/science/article/pii/S0920410598000771.

[46] A. Lang, J. Potthoff, Fast simulation of Gaussian random fields, 17 (3) (2011) 195–214 http://dx.doi.org/10.1515/mcma.2011.009.

[47] S. Zein, A. Laurent, D. Dumas, Simulation of a Gaussian random field over a 3D surface for the uncertainty quantification in the composite structures, Comput. Mech. 63 (6) (2019) 1083–1090, http://dx.doi.org/10.1007/s00466-018-1637-y.

[48] J. Karch, Improving on Adjusted R-Squared, Collabra: Psychol. 6 (1) (2020) 45, http://dx.doi.org/10.1525/collabra.343, arXiv:https://online.ucpress.edu/collabra/article-pdf/6/1/45/483406/343-4856-1-pb.pdf.

[49] S. Han, C. Wang, X. Liu, B. Li, R. Gao, S. Li, A random algorithm for 3D modeling of solid particles considering elongation, flatness, sphericity, and convexity, Comput. Part. Mech. 10 (1) (2023) 19–44, http://dx.doi.org/10.1007/s40571-022-00475-9.

[50] G.A. Kelesidis, S.E. Pratsinis, Determination of the volume fraction of soot accounting for its composition and morphology, Proc. Combust. Inst. 38 (1) (2021) 1189–1196, http://dx.doi.org/10.1016/j.proci.2020.07.055, URL https://www.sciencedirect.com/science/article/pii/S1540748920304879.

[51] A.G. Yazicioglu, C.M. Megaridis, A. Campbell, K.-O. Lee, M.Y. Choi, Measurement of fractal properties of soot agglomerates in laminar coflow diffusion flames using thermophoretic sampling in conjunction with transmission electron microscopy and image processing, Combust. Sci. Technol. 171 (1) (2001) 71–87, http://dx.doi.org/10.1080/00102200108907859, arXiv:https://doi.org/10.1080/00102200108907859.

[52] L. Zhao, S. Zhang, D. Huang, X. Wang, A digitalized 2D particle database for statistical shape analysis and discrete modeling of rock aggregate, Constr. Build. Mater. 247 (2020) 117906, http://dx.doi.org/10.1016/j.conbuildmat.2019.117906, URL https://www.sciencedirect.com/science/article/pii/S0950061819333598.

[53] C. Costa, P. Menesatti, G. Paglia, F. Pallottino, J. Aguzzi, V. Rimatori, G. Russo, S. Recupero, G. Reforgiato Recupero, Quantitative evaluation of Tarocco sweet orange fruit shape using optoelectronic elliptic Fourier based analysis, Postharvest Biol. Technol. 54 (1) (2009) 38–47, http://dx.doi.org/10.1016/j.postharvbio.2009.05.001, URL https://www.sciencedirect.com/science/article/pii/S0925521409000921.

[54] J. Kennedy, R. Eberhart, Particle swarm optimization, in: Proceedings of ICNN'95 - International Conference on Neural Networks, Vol. 4, 1995, pp. 1942–1948, http://dx.doi.org/10.1109/ICNN.1995.488968, vol.4.

[55] L. Théodon, C. Coufort-Saudejaud, A. Hamieh, J. Debayle, Morphological characterization of compact aggregates using image analysis and a geometrical stochastic 3D model, in: 2023 IEEE 13th International Conference on Pattern Recognition Systems (ICPRS), 2023, pp. 1–7, http://dx.doi.org/10.1109/ICPRS58416.2023.10179036.

[56] P.A. Cundall, O.D.L. Strack, A discrete numerical model for granular assemblies, Géotechnique 29 (1) (1979) 47–65, http://dx.doi.org/10.1680/geot.1979.29.1.47, arXiv:https://doi.org/10.1680/geot.1979.29.1.47.

[57] B.R. Kent, Meshes, models and textures, in: 3D Scientific Visualization with Blender®, in: 2053-2571, Morgan & Claypool Publishers, 2015, pp. 3–1 to 3–9, http://dx.doi.org/10.1088/978-1-6270-5612-0ch3.

[58] J.S. Brauchart, P.J. Grabner, Distributing many points on spheres: Minimal energy and designs, J. Complexity 31 (3) (2015) 293–326, http://dx.doi.org/10.1016/j.jco.2015.02.003, URL https://www.sciencedirect.com/science/article/pii/S0885064X15000205, Oberwolfach 2013.

[59] B. Keinert, M. Innmann, M. Sänger, M. Stamminger, Spherical fibonacci mapping, ACM Trans. Graph. 34 (6) (2015) http://dx.doi.org/10.1145/2816795.2818131.

[60] Q. Du, V. Faber, M. Gunzburger, Centroidal voronoi tessellations: Applications and algorithms, SIAM Rev. 41 (4) (1999) 637–676, http://dx.doi.org/10.1137/S0036144599352836, arXiv:https://doi.org/10.1137/S0036144599352836.

[61] J.M. Augenbaum, C.S. Peskin, On the construction of the voronoi mesh on a sphere, J. Comput. Phys. 59 (2) (1985) 177–192, http://dx.doi.org/10.1016/0021-9991(85)90140-8, URL https://www.sciencedirect.com/science/article/pii/0021999185901408.

Léo Théodon, an Engineering Ph.D. student at École des Mines de Saint-Étienne, specializes in computer science, data science, and image processing. His professional experience includes software development, modeling in scientific and construction sectors, and freelance consulting in BIM and structural calculation.

Carole Coufort-Saudejaud, a distinguished Maître de conférences at Toulouse INP-ENSIACET since 2006, specializes in environmental process engineering. Her expertise, honed through roles at INSA Toulouse and doctoral research on flocculation dynamics, cements her as a respected figure in the field of industrial process engineering.

Johan Debayle, esteemed Full Professor at MINES Saint-Etienne, specializes in Image Processing and Analysis. His career includes leadership roles at CNRS, honors as a Knight in the French Order of Academic Palms, and contributions as an Adjunct and Visiting Professor in Indonesia, highlighting his international recognition in the field.